HAL
open science

Distribution and intensity of water ice signature in South Xanadu and Tui Regio

Maélie Coutelier, Daniel Cordier, Benoît Seignovert, Pascal Rannou, Alice Le Gall, Thibaud Cours, Luca Maltagliati, Sébastien Rodriguez

To cite this version:

Maélie Coutelier, Daniel Cordier, Benoît Seignovert, Pascal Rannou, Alice Le Gall, et al.. Distribution and intensity of water ice signature in South Xanadu and Tui Regio. Icarus, 2021, 364 (August), pp.114464. 10.1016/j.icarus.2021.114464 . insu-03194788

HAL Id: insu-03194788

https://insu.hal.science/insu-03194788v1

Submitted on 15 Apr 2021

HAL is a multi-disciplinary open access archive for the deposit and dissemination of scientific research documents, whether they are published or not. The documents may come from teaching and research institutions in France or abroad, or from public or private research centers.

L'archive ouverte pluridisciplinaire **HAL**, est destinée au dépôt et à la diffusion de documents scientifiques de niveau recherche, publiés ou non, émanant des établissements d'enseignement et de recherche français ou étrangers, des laboratoires publics ou privés.

Journal Pre-proof

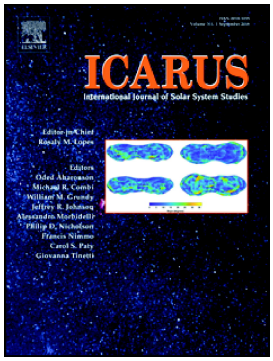

Distribution and intensity of water ice signature in South Xanadu and Tui Regio

Maélie Coutelier, Daniel Cordier, Benoît Seignovert, Pascal Rannou, Alice Le Gall, Thibaud Cours, Luca Maltagliati, Sébastien Rodriguez

PII: S0019-1035(21)00146-9

DOI: https://doi.org/10.1016/j.icarus.2021.114464

Reference: YICAR 114464

To appear in: *Icarus*

Received date: 10 July 2020

Revised date: 12 March 2021

Accepted date: 31 March 2021

Please cite this article as: M. Coutelier, D. Cordier, B. Seignovert, et al., Distribution and intensity of water ice signature in South Xanadu and Tui Regio, *Icarus* (2021), https://doi.org/10.1016/j.icarus.2021.114464

This is a PDF file of an article that has undergone enhancements after acceptance, such as the addition of a cover page and metadata, and formatting for readability, but it is not yet the definitive version of record. This version will undergo additional copyediting, typesetting and review before it is published in its final form, but we are providing this version to give early visibility of the article. Please note that, during the production process, errors may be discovered which could affect the content, and all legal disclaimers that apply to the journal pertain.

© 2021 Published by Elsevier Inc.

Journal Pre-proof

Distribution and intensity of water ice signature in South Xanadu and Tui Regio

Maélie Coutelier[a], Daniel Cordier[a], Benoît Seignovert[b], Pascal Rannou[a], Alice Le Gall[c,d], Thibaud Cours[a], Luca Maltagliati[e] and Sébastien Rodriguez[f]

[a] *Groupe de Spectrométrie Moléculaire et Atmosphérique - UMR CNRS 7331 Campus Moulin de la Housse - BP 1039 Université de Reims Champagne-Ardenne 51687 REIMS – France*

[b] *Université de Nantes, Univ Angers, CNRS, LPG, UMR 6112, F-44000 Nantes, France*

[c] *LATMOS/IPSL, UVSQ Université Paris-Saclay, Sorbonne Université, CNRS, Paris, France*

[d] *Institut Universitaire de France (IUF), Paris, France*

[e] *Nature Publishing Group, London, United-Kingdom*

[f] *Université de Paris, Institut de physique du globe de Paris, CNRS, F-75005 Paris, France*

ARTICLE INFO

Keywords:

Titan

Radiative Transfer

River channels

Water Ice

VIMS

Abstract

Titan's surface was revealed by *Cassini*'s instruments, showing the presence of liquid hydrocarbons in lakes, and features like dry riverbed. In order to study the sediment transport in Titan's channels and to map distribution of the water-ice signature in these terrains, we use a radiative transfer model to retrieve the surface albedo, after we estimated VIMS error with an original method. We also establish a criteria related to the intensity of the water ice signature. The

ORCID (s):

Journal Pre-proof

tuning of the radiative transfer model shows that the fractal dimension of Titan's aerosols is higher than previously thought, around 2.3 - 2.4. We find spots of high signal of water ice downstream, at the margins of Tui Regio, that could correspond to alluvial fans, deltas or crater rims. We also observe a very low water ice signal on Tui Regio, with a positive gradient between the central region and the boundary of the area, possibly due to the thickness variation of an evaporitic layer. The riverbeds show within the error bars a decreasing grain size from the top to the bottom of the channels. This reinforces the hypothesis of sediment transport via these river channels.

1. Introduction

Titan, the biggest moon of Saturn is one of the most complex moon of the Solar System, with dense atmosphere, hydrocarbon cycle, and water-ice crust. Titan has been targeted by two major space missions: *Voyager I* (1980) and *Cassini-Huygens* (2004-2017), and is still the subject of many studies. Lakes and seas of liquid hydrocarbons were discovered by *Cassini*'s ISS and RADAR in Titan's polar regions (Stofan et al., 2007; Turtle et al., 2009). The RADAR instrument also revealed in equatorial regions geomorphological structures related to the presence of liquid, like fluvial valleys incised in the *bedrock*, and alluvial fans (Le Gall et al., 2010; Birch et al., 2016). The existence of evaporitic terrains where also suggested (Barnes et al., 2011; Cordier et al., 2013; MacKenzie et al., 2014), often in place of paleo-sea (Moore and Howard, 2010). Water ice signature is not ubiquitous on Titan, contrary to most of Saturn's and Jupiter's moons, like Encelade and Europa. It was detected with *Cassini*'s Visual and Infrared Mapping Spectrometer (VIMS) in Titan's infrared dark region, often at the transition between dark and bright unit, and mixed with a dark material (McCord et al., 2006; Soderblom et al., 2007; Brossier et al., 2018). Griffith et al. (2019) also highlighted an equatorial corridor of possibly exposed water-ice using a principal component analysis (PCA) technique applied on VIMS data, showing a large scale terrains with low and high water ice content. While PCA is extremely useful for large data sets, and to study weak feature, it is not as detailed as a radiative transfer modeling and can not be used to retrieve quantitative information.

Barnes et al. (2007) have studied the channels of Mabon Macula using a combination of Synthethic Aperture Radar Image (SAR) and VIMS measurements. They find that the spectral signals of the channels share characteristics with Titan's "dark blue" terrains according to the adopted color composition. The considered terrains show an enrichment in water ice (Brossier et

Journal Pre-proof

al., 2018; Rodriguez et al., 2006) and the presence of benzene. These dark blue areas should result from the transport of material eroded from the mountains by the channels.This has been confirmed by Langhans et al. (2012) and Brossier et al. (2018). The latter studied the "dark blue" terrains found with VIMS on Titan. They used an accelerated version of radiative transfer model with precalculated tables to compare the spectral variations of different terrains. The IR-blue units were found to be enriched in water-ice (20 to 50 %), even if it is not the main component. Brossier et al. (2018) also described different types of IR-blue units. First, they have identified outwashed plains that are located between IR-bright terrains and dune field, created by sediments transported from mountain IR-bright units. Secondly, they found patches of IR-blue units located inside IR-bright terrains, produced by the erosion of these mountainous terrains. The last type is the ejecta blanket from impact craters. They also found that rivers are IR-blue, probably enriched in water-ice pebbles as well.

We focused our study on Titan's river bed, where the erosion due to liquid hydrocarbon could have revealed the bedrock, and where we could have clues on the sediment transport. Here we propose a study of the water ice signal distribution in South Xanadu and Tui Regio, where there are river channels (Le Gall et al., 2010), paleo-seas of hydrocarbons (Hofgartner et al., 2020), and terrains classified as IR-blue patches by Brossier et al. (2018). We employ a photometric analysis combined with an original method based on indicators to characterize the relative strength of the water-ice signature on the chosen VIMS cubes.

We focused on two radar bright channels investigated by Le Gall et al. (2010), larger than those reported by (Barnes et al., 2007) in Mabon Macula. These channels are located south of Xanadu, emerging directly from a mountain range. They are at the north of the evaporitic region Tui Regio (MacKenzie and Barnes, 2016). They form dry dendritic fluvial valleys (Langhans et al., 2012), with a width up to 8 km. Some areas studied in this work have also been investigated by Griffith et al. (2019), where evaporitic terrains were classified as ice-poor.

2. Radar and Infrared Observations

To investigate our region of interest, we used two complementary instruments of the *Cassini*'s mission: the RADAR, and VIMS.

Cassini's RADAR had four different modes: it could operate as a SAR, scatterometer, altimeter and radiometer at a wavelength of 2.2 cm. In SAR mode, it provided images of the

surface that are sensitive to local slope and terrains roughness: smooth surfaces appear dark while rough terrains are radar-bright. About 70% of Titan's surface has been mapped with this mode with a resolution ranging between 300 m/pixel and 4 km/pixel, revealing channels, lakes, mountains and dune fields.

VIMS Infra-Red instrument onboard *Cassini* scanned in a spectral range from 0.88 μm to 5.12 μm. In Titan's case, due to the methane absorption, VIMS could only observe the surface in 7 atmospheric windows centered at 0.93, 1.08, 1.27, 1.59, 2.01, 2.78 and 5 μm (Sotin et al., 2005; Barnes et al., 2005). Parts of the spectrum not located in an atmospheric window are called *bands*. As the RADAR spatial resolution was higher than VIMS, the SAR map allows a better characterization of geomorphologic structures in VIMS cubes.

The radar-bright river channels from Le Gall et al. (2016) have been imaged during the T44 flyby (2008-28-05) using SAR mode. We employed the T44 SAR image to select VIMS images overlapping these channels. Among them, we chose the cubes with the highest resolution in this area. Only two cubes have a pixel scale smaller than 18 km/pixel (see Tab. 1 and Fig. 1), which is twice the width of the bright channels. A weaker resolution may not contain enough channel signal to be distinguished. The first cube 1590648776_1 (labeled C15 hereafter) was acquired in 2008 during the same flyby as our reference radar swath. For this cube, VIMS was configured in High Resolution mode which increases the spatial resolution in the samples direction. The second cube (C18 hereafter) was taken in normal mode 7 years later in 2015 during the T111 flyby. For C18 we do not work with the entire cube, only a square made of 38 rows of samples and lines located in our region of interest. These cubes were calibrated with the RC19 calibration published by Clark et al. (2018)[1], using ISIS3[2] USGS tools. They are available at the *Cassini VIMS Data Portal*[3] (Le Mouélic et al., 2019). The navigation of the VIMS-IR cubes were computed using the latest C-smithed kernels (December 2017) and the python SpiceyPy toolkit (Annex et al., 2020). We took into account the offseted pointing boresight and the corrected initial scan mirror sample position for cubes acquired in HighRes mode, as recently reported by Nicholson et al. (2020).

[1] https://pds-imaging.jpl.nasa.gov/data/cassini/cassini_orbiter/vims-calibration-files/

[2] https://isis.astrogeology.usgs.gov/

[3] https://vims.univ-nantes.fr

Journal Pre-proof

Where changes exist, they are about 1 normal VIMS pixel compared to the original ISIS navigation and within the expected accuracy of the Cassini kernels ($\sim$0.12 mrad).

Table 1

VIMS cubes details. C15 And C18 are used in the study of the bright channels, while C14 is employed to test the validity of the model at *Huygens* landing site.

Cube number	Name in the text	Flyby	Date (DD-MM-YYYY)	Exposure (ms)	Mean ground resolution	Size (Samples x Lines)	Purpose
1590648776_1	C15	T44	28-05-2008	325	15 km/pxl	(28 x 14)	Bright channels
1809727868_1	C18	T111	07-05-2015	122	14 km/pxl	(64 x 64)	Bright channels
1481624349_1	C14	TB	13-12-2004	160	16 km/pxl	(24 x 12)	Model test

[[Image]]

Figure 1: Grey-scale: (a) RADAR swath containing the T48 and T44 flyby (Le Gall et al., 2010). (b) Annotated RADAR map, with footprints of VIMS cube 1590648776_1 (C15, blue) and 1809727868_1 (C18, orange). Purple lines: the rivers bright channels on which we focus our study. Tui Regio is roughly delimited in yellow, Xanadu mountains are similarly delimited in red, and the units defined by Lopes et al. (2019) and Moore and Howard (2010) are annotated in cyan. Green dots: channels that end in fan (Radebaugh et al., 2018). Blues lines: areas of high water-ice signal. The row of dark spots cutting the map vertically in half comes from HiSAR data, where the surface resolution is lower than SAR data. As an other useful central portion of this map comes from HiSAR data, we have chosen to keep the complete map instead of working only with SAR flyby.

C15 and C18 are re-projected in a equirectangular view for better viewing and comparison purpose in Fig. 2, with a color composition similar to that of Barnes et al. (2007).

Journal Pre-proof

[[Image]]

Figure 2: Equirectangular projection of (a) C15 and (b) C18 using Barnes et al. (2007), Baines, Clark and Nicholson] colors: 5.0 μm as red, 2.00 μm as green, and 1.29 μm as blue. This composition highlights evaporites in bright peach, sand in dark brown, enhanced water ice signal in dark and light blue.

3. The Radiative Transfer Model

In order to retrieve and study the surface albedo in different areas of interest from VIMS-IR spectra, we used a model of photometry inherited from Rannou et al. (2010, 2016). We first defined the average scattering and absorption features of the atmosphere, derived from the properties of its different components (particles, gases), as a function of wavelength and altitude. These optical properties were cast under appropriate forms to be used by radiative transfer (RT) solvers. This model depends on free parameters including surface albedo.

3.1. Atmospheric properties and composition

Most of Titan's atmospheric properties are known from *Cassini* and *Huygens* observations. The atmosphere temperature and pressure vertical profiles have been measured *in situ* by the Huygens Atmosphere Structure Instrument (HASI) (Fulchignoni et al., 2005) during *Huygens* probe descent into Titan's atmosphere. The methane mixing ratio has been measured by the Gas Chromatograph Mass Spectrometer (GCMS) onboard *Huygens* (Niemann et al., 2005, 2010). Isotopic ratios of CH_3D and $^{13}CH_4$ are those published by Nixon et al. (2012) (see table 2). For CO, HCN and C_2H_2 mixing ratios and vertical profiles (see table 2), we used results derived from CIRS observations (Vinatier et al., 2015, also available in VESPA database[4]), extrapolated for the low stratosphere and troposphere, and limited by the saturation vapor pressure.

3.2. Gas spectroscopic absorption

Molecular spectroscopic data (table 2) are mainly provided by HITRAN[5] database

[4] http://vespa.obspm.fr/planetary/data/

[5] https://hitran.org

(Rothman et al., 2013), with a notable exception for CH_4 and its isotopes CH_3D and $^{13}CH_4$ for which we employed the up-to-date theoretical line lists computed by Rey et al. (2017, 2018). These data are publicly available at the Theoretical Reims-Tomsk Spectral database[6] (Rey et al., 2016). Following de Bergh et al. (2012) for the line broadening, we represented the line profiles by a Voigt function with a cut-off at 26 cm^{-1} from the line center. They were then modified with a sublorentzian decay with a wavenumber characteristic length of 120 cm^{-1} for all species except CO. For the latter, we used the specific cut-off recommended by Lellouch et al. (2003). As VIMS channels wavelengths change through the mission, we followed Clark et al. (2018) recommendations and calculated the spectroscopic absorption consequently.

Table 2

List of CH_4 isotopes ratio taken into account, from Nixon et al. (2012), and other absorbing gases mixing ratio derived from CIRS observations (Vinatier et al., 2015).

Methane	Isotope ratio	Absorbing gaz	Mixing ratio
D/H	$1{,}59\times10^{-4}$	CO	3.3×10^{-4}
$^{12}C/^{13}C$	86,5	C_2H_2	4×10^{-4}
CH_3D/CH_4	$6{,}36\times10^{-4}$	HCN	3×10^{-7}
$^{13}CH_4/CH_4$	$1{,}156\times10^{-2}$		

3.3. Aerosol model

Considering the previous works of Tomasko et al. (2008) and Doose et al. (2016), we divided the aerosols altitude distribution into two layers (see Fig. 3). The upper haze layer extends from the tropopause at 55 km to the top of the atmosphere. It is composed of photochemical aerosols assumed to be fractal aggregates. The lower layer, hereafter called *mist*, is an undefined mixture of condensed material and photochemical haze.

To model the haze optical properties such as the single scattering albedos and the extinction cross-sections, we adopted the scattering model for fractal aggregate developed by

[6] `https://theorets.tsu.ru` and `https://theorets.univ-reims.fr`

Journal Pre-proof

Rannou et al. (1997). The aerosol phase functions that we use are adapted for the backscattering. The preliminary analysis of a sequence of VIMS observations of Titan acquired in November 2012 (flyby T88) led to propose a modification of the aerosol phase function initially recommended by Doose et al. (2016). During this 5-min long sequence, VIMS acquired 26 consecutive datacubes over the same location, but with varying emission and phase angles. In order to keep the haze opacity constant over the 26 datacubes, one had to change the aerosol phase functions by adding 20% more of backscattering at all wavelengths. We used these modified aerosol phase functions in the present study. A comprehensive analysis of these observations is out of the scope of the present article, but will be soon subject to a separate dedicated article.

This model allows us to study different morphology of aggregates, whereas Tomasko et al. (2008) phase functions are only valid for a restricted set of parameters (*i.e.* a fractal dimension of 2 and 3000 monomers of 50 nm). In our model, we keep the fractal dimension as a free parameter. The aerosols refractive indices were derived from those published by Rannou et al. (2010). They were adapted to fit the haze single scattering albedo in agreement with the prescription proposed by Doose et al. (2016). Since mist particles remain poorly known, we made no differences between haze and mist particles phase functions. The haze and mist extinction $k(z,\lambda)$ spectral slopes were obtained with this scattering model, because Doose's results based on the Descent Imager / Spectral Radiometer (DISR) data from *Huygens* probe are only available between $\sim$ 0.4 and 1.6 μm.

Consistently, our mist scattering albedo ω_{mist} follows Doose et al. (2016) prescription, i.e. $\omega_{mist} = (0.565 + \omega_{haze})/1.5$. Similarly, the transition altitude between "mist scattering regime" and "haze scattering regime" and the vertical extinction profile $k(z,\lambda)$ came from the same source.

The haze and mist optical depths were scaled with respect to the optical thickness obtained by Doose et al. (2016) at 1 μm. Those profiles were adjusted thanks to a minimization procedure with two free parameters: F_h for the haze, and F_m for the mist, allowing for different ratios for the haze and mist. As a consequence, the haze and mist opacity at an altitude z and a wavelength λ are:

$$\Delta\tau_h(z,\lambda) = F_h \Delta\tau_{h_D}(z) \frac{\sigma(\lambda)}{\sigma(\lambda_0)} \tag{1}$$

$$\Delta\tau_m(z,\lambda) = F_m \Delta\tau_{m_D}(z)\frac{\sigma(\lambda)}{\sigma(\lambda_0)} \tag{2}$$

with $\sigma(\lambda)$ the extinction cross-section of fractal aggregates, $\Delta\tau_{h_D}(z)$ and $\Delta\tau_{m_D}(z)$ the normalized haze or mist opacity of Doose at 1 μm for an atmospheric layer at the altitude z times the total opacity of the atmospheric column at $\lambda_0 =$ 1 μm.

3.4. Other components and technical aspects

The scattering coefficients due to Rayleigh scattering were derived from equations (2.30) and (2.31) of Hansen and Travis (1974). They adapted to Titan's atmosphere using the CH_4 column density. Our model also includes N_2-N_2 and N_2-H_2 collision-induced absorption (CIA) (Lafferty et al., 1996; McKellar, 1989). Titan's surface is assumed to scatter as a lambertian surface.

We discretized the atmosphere into 70 layers uniformly distributed from ground level up to an altitude of 700 km, since it was found as an acceptable compromise between accuracy and computation time (McKay et al., 1989; Cours et al., 2020). In addition, for each layer we computed the average optical depths, phase functions and single scattering albedos for all VIMS-IR channels. We have the choice between two solvers to solve numerically the radiative transfer equations: `SHDOMPP` developed by K. Evans[7] (Evans,2007) that runs in a plan-parallel approximation, and `SPSDISORT` from the library libRadtran[8] (Mayer and Kylling, 2005; Emde et al., 2016) that includes a pseudo-spherical geometry. The first solver was found to compute ten times faster thanthe second, which has a wider validity range since it includes spherical corrections. The optical depths of the different gases were calculated according to the correlated-k approximation (Goody et al., 1989), including four terms for each channel to represent the opacity of the gases.

In radiative transfer models such as `SHDOMPP` or `SPSDISORT`, the phase functions have to be expanded on a basis of Legendre polynomials, and we use 100 terms. In the model, radiance is calculated for a given number of directions (that is, streams). The resolution and computation

[7] `http://coloradolinux.com/shdom/shdomppda/`

[8] `http://www.libradtran.org/doku.php`

Journal Pre-proof

time increase with the number of streams. The section 5.1 treats in details the optimal number of streams to use in the model.

The synthetic spectra were fitted to observational data in the bands using the Levenberg-Marquardt algorithm (Levenberg, 1944; Marquardt, 1963). For that purpose we employed the implementation of this method available under the form of the LMDIF subroutine, part of the `MINPACK` library (Moré et al., 1980) written in `FORTRAN`.

Table 3

List of gaseous species accounted for in our radiative transfer model.

Species	Instrument	Spectrum
CH_4	GCMS	TheoReTS
CH_3D	CIRS/GCMS	TheoReTS
$^{13}CH_4$	CIRS/GCMS	TheoReTS
CO	CIRS	HITRAN
C_2H_2	CIRS	HITRAN
HCN	CIRS	HITRAN

[[Image]]

Figure 3: Sketch of the atmospheric profile we assumed in this work. Fractals are from Botet et al. (1995), and this illustration is from Seignovert and Rannou (2019). According to the adopted global picture, a low altitude layer, extending from the ground to 55 km, is filled by a misty air containing more or less methane-wet particles. This first layer is topped by a less dense but more extended region of haze settled by fractal particles. In our model, these particles are assumed to be made of 3000 monomers, each with an individual radius of 50 nm, the adopted fractal dimension is $\mathcal{D}_f = 2.3$. The single-scattering albedo ω_{mist} of mist *particles-droplets* has been scaled to the single-scattering albedo ω_{haze} according to the law: $\omega_{mist} = (0.565 + \omega_{haze})/1.5$ (Doose et al., 2016).

4. On the error of VIMS

Journal Pre-proof

The photometric uncertainties in VIMS calibrated cubes are not well known, and depend on the considered channel (Brown et al., 2004). Sromovsky and Fry (2010) established a global average error of 2.5% of the I/F values, with an I/F offset error of 5×10^{-4}. In order to provide a more accurate description of the instrument noise, we developed a new method based on the analysis of inter-pixels variability. With this method we can estimate combined errors due to the instrument, data calibration and post treatment. Assuming a slow pixel to pixel variation, we perform an estimate of the intrinsic variability of adjacent pixels.

First, for a given data cube, we chose about 10 pixels evenly distributed over the image. We took into account the 8 first neighbors around them, forming a 3×3 box around the selected pixel. For each set of 9 pixels, we calculated at each wavelength the mean $\overline{I/F}$ and standard deviation σ. Finally we derived an estimator of the relative standard deviation Σ of each 9-pixels set:

$$\Sigma = \mathrm{std}(I/F)/\mathrm{mean}(I/F) \tag{3}$$

For C15 and C18, we calculated Σ for the whole spectrum as we need it to estimate the surface albedo error bars. The results are represented by dots in Fig. 4-a. The method is only strictly valid in the bands because in the windows we get a variability of the signal related to the natural variability of the surface. We calculated Σ in the atmospheric windows for comparison purpose. The geometry changes between each pixels and can influence the retrieved Σ. This will be corrected by another step of the method.

By analyzing different set of pixels, over a few images, we can first notice in Fig. 4-a that Σ depends on the cube and the wavelength. We determined specific profiles of Σ for each image of interest. They were chosen manually, following the general shape of the results (Σ_1 and Σ_2 uncorrected in Fig. 4-a for C15 et C18 respectively). We chose to cap Σ below 2.5 μm and at 5 μm by a high value so we do not underestimate the error bars. To obtain the uncorrected Σ in atmospheric windows, we interpolate the uncorrected Σ of adjacent bands.

We then determined the error due to variations in viewing geometry from one pixel to an other. We obtained it with the same method, but instead of the cube spectra, we used synthetic spectra with fixed parameters for the surface albedo and the aerosols. For these synthetic spectra, only incidence and emergence angles change, similarly as those of the cube. In that way, the only differences in I/F between pixels of the same cube are due to angle variations. With the

differences in incidence and emergence angles between C15 and C18, the thickness of the atmosphere layer crossed by the beams is greater for C18 than for C15. As a result, contrary to C18 where incident angles are higher, the error due to angle variations is lower in the bands for C15.

We subtracted from our previous profiles the Σ due to angle variation. Final profiles of Σ are shown in Fig 4-b. Here Σ_1 is adapted for C15, whereas the profile Σ_2 is adapted for C18. Theoretically, in the bands we should have a negligible influence from the surface. In Fig. 4-a for C15 and C18 (red and blue points) we tend to have a lower Σ in the windows. VIMS uncertainties depend on the number of photons. The greater I/F, the smaller uncertainties. Because of the interpolation of $\Sigma_{1,2}$ uncorrected for the windows, we may overestimate the error in the atmospheric windows where we have a greater I/F than in the bands.

The corrected Σ for C15 and C18 in Fig. 4-b show the influence of incident and emergent angles. The corrected Σ for C15 is higher in the windows than in the bands, under 2 μm. For C18 it is slightly lower, except at 5 μm. Generally, there is an enhanced variability and error around 2.35 μm, and beyond 3 μm. Our results there are quite different from the 2.5% estimated by Sromovsky and Fry (2010), but below 2 μm the values are of the same order in the windows. The influence of the temperature inside VIMS, causing IR radiation, is greater at large wavelengths. That could partly explain the increasing uncertainties with the wavelength. The low number of photons at greater wavelength is also another factor.

[[Image]]

Figure 4: (a) Chosen spectral profiles of Σ (lines), and retrieved values of Σ (points) for C15 (red) and C18 (blue). Titan's atmospheric windows are in gray rectangles. (b) Final spectral profiles of Σ (lines) for the C15 (Σ_1) and C18 (Σ_2), where we subtracted from our previous uncorrected profiles the Σ due to the angle variation (dots).

These Σ are significant in the bands up to 2.5 μm for the calculation of the χ^2 and the minimization of the function $\mathcal{Y}$ used to retrieve atmospheric parameters F_h and F_m, the scaling factors for the haze and the mist:

Journal Pre-proof

$$\mathcal{Y}_n = \frac{|(I/F)_n^{obs} - (I/F)_n^{mod}|}{\Sigma_n \times (I/F)_n^{obs}} \tag{4}$$

$$\chi^2 = \frac{1}{N}\sum_{n=1}^{N}\mathcal{Y}_n^2 \tag{5}$$

with N the number of channels we used to determine the parameters, I/F_{obs} the observed I/F and I/F_{mod} the modeled I/F. Σ_λ is also used later to estimate the albedo error bars.

Once surface albedos are determined for each channel, we can finally evaluate the uncertainties of the surface albedo for a wavelength λ. We need the values of Σ_λ previously calculated and the derivative of the albedo A_λ with respect to I/F_λ:

$$\sigma_{A_\lambda} = \left|\frac{dA_\lambda}{dI/F_\lambda}\right|\Sigma_\lambda \tag{6}$$

These errors will be used to calculate our results uncertainties.

5. Test and preparation of the model for surface analysis

In this section we present sensitivity tests performed with the radiative transfer model, using `SPSDISORT` and `SHDOMPP`. The scope of this section is to define the number of stream used to discretize the intensity field in the model and to define the limit incident and emergent angles for using the parallel plane model beyond which we must account for the atmosphere sphericity. Then, we also describe how we set the atmosphere free parameters and our observed data fitting method.

5.1. Tests of the model against the number of streams

A solver for the radiative transfer equations calculates the intensity field in a finite number of directions for each atmospheric layer. This is what we call the number of streams. In order to optimize the model execution time, we tested the solvers accuracy with different number of streams. A high number of streams increases the accuracy, but also the execution time.

We define a testing case with fixed haze and mist parameters $F_h = F_m = 1$. The surface albedo is set at a uniform value of 0.05. We use a near-nadir viewing with an incidence angle of 3 $^\circ$, an emergence angle of 5° and a phase angle of 7°. Those are extreme conditions for the

SHDOMPP because the nadir configuration requires more accuracy, i.e. a higher number of streams than other geometries (Evans, 2007).

We set a reference with a simulation made with 100 streams, as we would never use a number so high due to the runtime, even if the accuracy of the results is better. We then compare the model performance with different number of streams. In order to estimate the minimum number of streams required to have less than 0.5% difference in I/F at each wavelength with the reference case, we start with 16 and we increase numbers by steps of 4 streams (Fig. 5). As the differences between the reference case and the tests decrease, the differences between the tests also decrease, allowing us to choose an optimum number of stream.

For the solver `SHDOMPP`, we have less than 1% difference when using more than 28 streams. With 32 streams the difference falls below the 0.5% limit. The solver `SPSDISORT` requires a minimum of 36 streams to have less than 0.5% difference compared to the 100-streams test case. In view of the results in Fig. 5, and taking into account the geometry and the increase of computation time with the number of streams, we decided to use for `SHDOMPP` a number of 32 streams up to 1.7 μm, and 24 streams for the rest of VIMS-IR wavelengths. For the `SPSDISORT`, we work with 40 streams up to 1.7 μm, and 24 streams for the reminder of the spectrum. Doing so, we have less than 0.5 % of difference with the reference test at each wavelength, with a smaller computation time. For example, for a cube made of 4096 pixels, the RT model using `SPSDISORT` has a runtime of less than 24 hours when using 500 processors.

[[Image]]

Figure 5: Differences in % between the I/F calculated with SHDOMPP (top panel) and SPSDISORT (bottom panel) with different number of streams compared to the results with 100 streams. Incidence: 3°, emergence: 5°, phase: 7°. The relative error is: $\Delta r = \left| \frac{I/F_{Nstr} - I/F_{100}}{I/F_{100}} \right|$.

5.2. Tests of the model in a spherical viewing

Barnes et al. (2018) consider as acceptable the use of parallel-plane approximation up to 60 $^\circ$ for incidence or emergence angles. In this work, we compared the results obtained respectively with SHDOMPP in a parallel-plane approximation and SPSDISORT in a pseudo-spherical

geometry at different incident angles (see Fig. 6). For this testing case, we use 32 streams for both models, and a emergence angle of 10°. We change the incidence angle from 10° to 80° with a 10° increment.

Fig. 6 shows that for incidence angles lower than 30°, we have differences between solvers smaller than 1%, which is in agreement with Barnes et al. (2018) result with a Monte-Carlo RT model. Errors reach more than 5% in Titan's atmospheric windows at 60°. Giving these results, we decided for our study to employ SHDOMPP with C15 (Fig. 13-a) when the incident angles are below 50°. For C18 (Fig. 13-b), we chose to work with SPSDISORT, as in our region of interest incidence angles go beyond 55°.

[[Image]]

Figure 6: Differences (%) between I/F calculated with `SHDOMPP` and `SPSDISORT` for different incidence angles. Emergent angle: 10°. Relative error: $\Delta r = \left| \frac{I/F_{SHD} - I/F_{SPS}}{I/F_{SPS}} \right|$

5.3. Haze and mist properties for surface analysis

The last step of the radiative transfer model setting consisted in defining the haze and mist properties that best reproduce the spectra in the bands, where surface has no influence. With our model, we retrieved haze and mist properties by fitting a spectrum taken in a dark tropical area of Titan in order to minimize the influence of surface. More specifically, we chose 16 test pixels where surface albedo is known to be extremely dark (Griffith et al., 2012), from the cube v1567239055, acquired on August, 31, 2007. In that way, we have set the model in such a way a negative value of the surface albedo is not possible even where surface albedo is especially low. VIMS uncertainties defined in section 4 were taken into account in the algorithm.

We used the standard case for aerosols morphology described in section 3.3. In Fig. 7 with a fractal dimension of $\mathcal{D}_f = 2$ we obtain a good fit except for the band around 1 μm. This is a recurring problem for each VIMS cube. To solve this problem we first performed several tests, using other tholins refractive index, varying the single scattering albedo with a constant factor, or using the condition $F_h = F_m$. However this did not improve the fit around 1 μm. We finally tested other values of fractal dimension.

Varying $\mathcal{D}_f$ has an impact on the spectral slopes of the haze and mist optical depths (see Fig. 8), and on the phase functions. We kept the number of monomers at 3000 since it was defined from the solar aurea with DISR, which depends in first place on the amount of grains, regardless the fractal dimension.

Then, in order to retrieve the surface albedo and the χ^2 (see Eq. 5) corresponding to each $\mathcal{D}_f$, the parameters F_h and F_m are set free to fit the data in the bands. We found that the fit is greatly improved with $\mathcal{D}_f >$ 2.0 in each of the selected pixels at short wavelengths (see Fig. 7 for one of the test cases), especially for the band around 1 μm, and between 1.8 and 2 μm. The χ^2 is generally reduced by a factor of 2 between $\mathcal{D}_f$ =2 (χ^2 = 250 in the example) and $\mathcal{D}_f$ =2.3 ($\chi^2 = 120$ in the example). We have obtained a better fit at 1 μm, at the short wavelength of the 1.6 μm window, and around 1.8-2.0 μm with $\mathcal{D}_f$ = 2.3- 2.4, than with $\mathcal{D}_f$ = 2 as proposed by Tomasko et al. (2008). The surface albedo is also impacted with the change of the fractal dimension. The slope of the surface albedo at 1.22 μm for $\mathcal{D}_f > 2.1$ is reversed and the shape at 1.55 μm is flatter even if the graphic scale tends to smooth the variations. Lastly, the surface albedo globally decreases when increasing fractal dimensions, except at 0.93 μm (Fig. 7-bottom).

To compare the total haze opacity with Doose et al. (2016) analytical model, we have chosen a test case with $F_h = F_m = 1$. The optical depths obtained in Fig. 8 for different fractal dimensions are adjusted for a better viewing. The differences of I/F at 1 μm in Fig. 7 are correlated with the variations of haze opacity τ as a function of wavelength in Fig. 8: the spectral slopes are a close equivalent to the one recommended by Doose et al. (2016) beyond $\sim$ 1.3 μm. Below this threshold, the smaller is $\mathcal{D}_f$, the steeper is the spectral slope. While opacity remains the same above 1.3 μm, fractal aggregates lead to a too large opacity at 1 μm for $\mathcal{D}_f$ = 2.0, and yield an opacity comparable to the expected opacity at $\mathcal{D}_f$ $\sim$ 2.3 - 2.4. As Fig.8 shows, $\mathcal{D}_f$ = 2.4 is a good candidate, but below 0.8 μm the result is less consistent with Doose et al. (2016) than for $\mathcal{D}_f$ = 2.3.

These results imply that aerosols are more compact than expected at least, at this location and date. They also imply that the fractal dimension value is between 2.3 and 2.4. This is the case

for C15 and C18 as well, as the fit is also improved for the pixels we have chosen to do the comparison with.

[[Image]]

Figure 7: Fits of the pixel (38,19) of the cube v1567239055, using different fractal dimension (top), and the corresponding surface albedo (bottom). Dotted lines: uncertainties for $\mathcal{D}_f$ = 2 and $\mathcal{D}_f$ = 2.4.

Based on these results, we decided for our study to employ a fractal dimension of 2.3, even if we obtain almost similar results with $\mathcal{D}_f$ = 2.4. As seen in Fig. 7, with $\mathcal{D}_f$ = 2.4 the fit is the best at 1 μm, but $\chi^2 = 150$ which is larger than for $\mathcal{D}_f$ = 2.3 ($\chi^2 = 120$), meaning that the fit is not as great at other wavelengths.

[[Image]]

Figure 8: Total haze opacity with F_h and F_m equal to 1, and angles of incidence and emergence at 10°, with different values of the fractal dimension. The curves follows the microphysics aerosol model from Rannou et al. (2004). Results are adjusted to fit Doose et al. (2016) curve at 2.88 μm

5.4. Tests of the final model on *Huygens* landing site

Thanks to *Huygens* probe, the aerosol vertical profile is known at *Huygens* landing site i.e., at 192.3°W 10.5°S Kazemnejad et al. (2011) on January, 14, 2005. To confirm the model validity, we ran a test on a cube containing *Huygens* landing site, and at a date close to *Huygens* landing day. For cubes respecting these criteria, the retrieved values of F_h and F_m should be close to 1 as we use the vertical extinction profile retrieved from *Huygens* given by Doose et al. (2016). The tests where made with our final model settings, $\mathcal{D}_f = 2.3$ and the stream number chosen in section 5.1. Incidence and emergence angles are in the validity domain of `SHDOMPP`.

The closest cube in time from *Huygens* landing date is the cube 1481624349_1 (labeled C14 hereafter), acquired with the High Resolution mode on December 13th, 2004, one month before the landing. We performed the RT analysis on the entire cube. Results for the haze and mist

parameters are presented in Fig. 9. The histogram scales are the same, for better comparison of the results. They show a distribution of the parameters F_m and F_h close to 1.1 for the case $F_h = F_m$ (Fig. 9-a) where the normalized vertical profile is equally multiplied. This result is good considering that we adjust the parameter using a larger wavelength range with VIMS-IR than for DISR, and that we do not have the same incident and emergent angles. The pixel (10,2) overlaps *Huygens* landing site, where the χ^2 from Eq. 5 is 90 for $F_m = F_h = 1.09$, and 75 for $F_h \neq F_m$ with $F_h = 1.08$ and $F_m = 1.24$. Having different haze and mist parameters thus leads to a better fit.

[[Image]]

Figure 9: (a) Histogram of retrieved haze and mist parameters for $F_h = F_m$ for the cube C14. (b,c) Histogram of retrieved haze and mist parameters respectively for the cube C14 for the case $F_h \neq F_m$. Results at *Huygens* landing site are indicated in red. The relative standard deviation is noted ΔF_h* in order not to be confused with Σ. (b)

There is no reason for having the same haze and mist parameters, so for the second test case, their values are allowed to be different. The resulting best-fit mean values are 1.22 for F_m (Fig. 9-b) and 1.09 for F_h (Fig. 9-c). The mist parameter is more dependent on the lower atmosphere, and is more variable than the haze parameter. This is why the result differs from the first test case. F_h is close to the previous test value while F_m differs, showing that the mist only plays a second order role in the model. Using two parameters instead of one thus results in a gain of information on the mist. The 10 % differences between Doose et al. (2016) values and ours are acceptable given the different initial data.

Since DISR instrument on board *Huygens* made the unique *in situ* measurement of a Titan's terrain albedo, we propose here a comparison between these observations and surface reflection coefficient obtained using our method on C14 cube. DISR wavelengths range is less extended than VIMS-IR, so the comparison is only possible below 1.6 μm (Schröder and Keller, 2008; Karkoschka et al., 2012).

In Fig. 10, we plotted our results derived form VIMS cubes against two DISR observations.

We can not compare the absolute albedos directly because of the different conditions like the pixel resolution (14 km for our cube *versus* a few meters at most for DISR after landing), and the geometry of incidence and emergence angles. In our model we assumed a lambertian surface with isotropic reflectivity, but *Huygens* landing site reflectivity is more complex and angle-dependent (Karkoschka et al., 2012; Karkoschka, 2016). We do not expect to obtain exactly the same surface albedo as the previous studies for these reasons. However, the global decreasing shape is similar, except at 1.08 μm. We also note at 1.55 μm a similar bowl shape of the albedo curve. The slight difference at 1.08 μm could mean that this pixel also contains absorbing material around 1.08 μm. It may also be due to a missing absorption in this window in our model, or a difference in the atmosphere properties, for a small change in the single scattering albedo of the mist has a greater effect at short wavelength ($<1.3\mu$m) (see the light blue results in Fig. 10). With an observed field much larger for VIMS, the chemical composition and spectra of considered terrains may be heterogenous for fields as large as ~ 100 km^2; explaining the differences that we have noticed. It could also be caused by the slight VIMS wavelength shift that is more noticeable in the firsts windows since they are much narrower. The differences occurs for other cubes taken in this area and close to the landing date, but not with cubes taken years later, maybe because of the shift.

[[Image]]

Figure 10: *Huygens* landing site surface albedo, derived from DISR and VIMS instruments. The surface albedo of pixel (10,2) in the cube C14 is retrieved for the cases $F_h = F_m$ (purple), $F_h \neq F_m$ (green) and for a case with the single scattering albedo (SSD) of the mist decreased by -0.03 (light blue). Results from Schröder and Keller (2008) (red) and Karkoschka et al. (2012) (dark blue), based on DISR dataset are indicated. Literature data are for a null phase angle. We approximately scaled them following Karkoschka et al. (2012) for a phase angle of 18°.

Globally, this VIMS/DISR comparison is reassuring even if, for above mentioned reasons, it cannot be considered as a formal validation of our approach.

6. Surface albedos of Xanadu and Tui regio

6.1. Method

To retrieve the surface albedo from VIMS pixel data, we fit the observed spectra in the methane bands by adjusting both scaling factor F_h and F_m, using the minimization method described in Sect. 4. Once the scaling factors are adjusted, we retrieve the surface albedo in the methane windows. Fig. 4-a shows the detailed windows. We routinely ran three simulations for each window, assuming a surface albedo of 0.05, 0.15 and 0.25, independently of the wavelength. For each VIMS channel sensitive to the surface, the surface albedo is finally determined by linear interpolation.

6.2. Criteria for water ice presence

Using VIMS spectra collected on Enceladus and shown in Fig.11-a, we determined the water ice absorptions. They are centered at 1.04, 1.27, 1.51, 2.03 and 3 μm. Titan's atmospheric windows are not exactly located where these absorptions occur, but they are influenced by them even when water ice absorptions are located at the edges of atmospheric windows.

[[Image]]

Figure 11: (a) Spectra of Enceladus, from 5 different VIMS cubes, (b) Experimental water-ice spectra with different grain size, from the GHOSST database. Grey columns represent the channels used to calculate the ratios. Their widths depends on the number of channels averaged.

Due to Titan's atmosphere strong absorptions, and because sedimented aerosols partly cover the surface, we do not expect a pure water-ice spectra on Titan. This is why we looked for traces and influence of the water-ice in Titan's surface spectra.We have then defined our criteria to measure the water ice signature on Titan. These criteria are based on a combination of conditions on the ratios between the water-ice absorption bands (Barnes et al., 2007; Robidel et al., 2020). Following the shape of the water ice spectrum, those mean and ratios values likely indicate the presence of water ice signature if:

- r_1 : $1.58/1.28 < 1$, as water ice absorbs more at 1.58 μm
- r_2 : $2.03/1.28 < 1$, as water ice absorbs more at 2.03 μm
- r_3 : $2.03/1.58 < 1$, as water ice absorbs more at 2.03 μm
- r_4 : $2.7/2.8 > 1$, as water ice absorbs more at 2.8 μm

- $\overline{A_5}$: Mean of the 5 μm window low as water ice spectrum is low at 5 μm compared to the rest of the spectrum.

We chose not to use the ratio $1.28/1.08$ (Barnes et al., 2007), which, according to the considered spectra of Enceladus (Fig. 11-a), can either be greater or lower than 1 - possibly because of impurities - even if in the pure water ice case from GHOSST[9] database (Fig. 11-b), the value of the ratio is strictly greater than 1. Not all ratios have the same impact: we tend to have greater error bars at short wavelengths for the albedo, and there are known missing absorptions (Cours et al., 2020), like for ethane at 2.7-2.8 μm (Maltagliati et al., 2015). Furthermore, we work with the VIMS data calibration RC-19 which is more recent, but less reliable for the 2.7-2.8 windows compared to the RC-17 as it tends to change the intensities values in this window by about 5 % (Clark et al., 2018). With the assumption that the effect of the missing ethane absorptions and the calibration is the same for each pixel, working in relative and not in absolute is acceptable. Even so, we chose to weight the ratios and mean by their known calculated uncertainties. For the mean albedo $\overline{A_i}$ of a window of N values, the uncertainties $\Delta\overline{A_i}$ is:

$$\Delta\overline{A_i} = \frac{1}{N}\sqrt{\sigma^2_{A_{i_1}} + \ldots + \sigma^2_{A_{i_N}}} \tag{7}$$

with σ_{A_i} the uncertainty of the surface albedo at a given wavelength (see Eq. 6). Then for each ratio $r = \overline{A_i} / \overline{A_j}$, the relative uncertainty of the ratio is:

$$\sigma_r = \frac{\Delta r}{r} = \frac{\Delta\overline{A_i}}{\overline{A_i}} + \frac{\Delta\overline{A_j}}{\overline{A_j}} \tag{8}$$

We defined a multi-criteria analysis parameter δ to estimate the presence of water ice. This parameter combines the relevant individual I/F ratios and the 5 μm mean previously mentioned. For the multi-criteria analysis, these ratios and 5 μm-mean are normalized between 0 and 1 with the following method. For a ratio r_1, the normalized ratio r_{1_n} is:

$$r_{1_n} = \frac{r_1 - r_{1_{min}}}{r_{1_{max}} - r_{1_{min}}} \tag{9}$$

With $r_{1_{min}}$ and $r_{1_{max}}$ the minimum and maximum values of the ratio for the considered

[9] https://ghosst.osug.fr/

Journal Pre-proof

cube. The normalized values are then added if the expected value of the non-normalized ratio or mean in case of pure water ice signature is greater than 1 (i.e. $r_{2.7/2.8}$). They are subtracted if the expected value is lower than 1 (i.e. all other ratios and 5 μ m-mean), as shown in equation 10. In this way, theoretically the highest possible value for δ is 1 indicating a prominent water ice-rich signature, and the lowest value is -4, for an extremely poor water-ice signal. In addition, the normalized ratios and mean at 5 μ m are weighted by (1- σ_r), with σ_r the relative error of each VIMS channels ratio r. We also set a lower limit for (1- σ_r) which cannot be lower than 0, even if it does not happen in our results. The parameter δ is explicitly:

$$\delta = -(1-\sigma_{A_5})\overline{A_{5_n}} + \sum_{k=1}^{4} \pm (1-\sigma_{r_k}) r_{r_k} \tag{10}$$

With $\overline{A_{5_n}}$ the normalized mean surface albedo at 5 μ m, and k the number of the normalized ratio r_n. δ increases when the probability of water ice presence increases. With Eq. 7 and 8, we are able to establish our ratios' error, and determine which results are relevant. With ratios weighted by their uncertainties, -4 and 1 are ideal values that can not be obtained. Furthermore, δ must not be interpreted alone since it is obtained using normalized values: there is no specific threshold value of δ which define is indeed water ice or not. It shows subtle changes in the surface composition. The possible results consistency between the cubes reinforces the interpretation. We also need VIMS colormaps and the RADAR map to scout the terrains beforehand and to better interpret the results. The criteria δ should be considered as an indicator of the strength of the water ice signature and not as a direct estimator of water ice abundance. It should be regarded as a tool for terrain classification.

6.3. Haze and mist results

[[Image]]

Figure 12: Maps of the haze and mist coefficients for C15 (a) and (c) respectively, and for C18 (b) and (d) respectively, overlaid to the RADAR map.

Fig. 12 shows F_h and F_m regional variation in C15 and C18, overlaid on the RADAR

map. Each point corresponds to a cube pixel. The haze factor seems to be more stable than the mist factor, which is expected since the mist factor should be more sensitive to local atmospheric variations on the surface. Both factors are not correlated, but we note a correlation with the incident and emergent angles in Fig 13. C15 coefficient F_h (Fig. 12-a) is uncorrelated, but F_m in C18 (Fig. 12-d) seems to be correlated with the emergent angles, while F_m in C15 and F_h in C18 (Fig. 12 c and b) appear to be anti-correlated with the incident angles. Yet, as no regular pattern stands out, there is no argument for an actual correlation between the angles and the haze and mist parameters values.

[[Image]]

Figure 13: (a) Pixel footprints of the VIMS cube 1590648776_1. Colors are mapped with VIMS spectral channels ratios: $1.58/1.28$ as red, $2.03/1.28$ as blue, $1.28/1.08$ as green, with contourlines corresponding to the incident angles (orange lines) and emergence angles (blue lines). (b) Similar figure for the VIMS cube 1809727868_1. This color code highlights water ice in dark blue.

We acknowledge a *bias* in our model: the atmosphere is assumed to be laterally homogeneous and infinite with no change of the aerosols vertical profile, whereas in our results the parameters F_h and F_m change for each pixels. However the *bias* is small, as at most rays go through 5 different columns of atmosphere before reaching the ground pixel for C15, and 8 for C18, and the values of the haze and mist parameters do not change in a significant manner within 5 or 8 adjacent pixels. The model can be tuned with free parameters but the haze and mist vertical profiles, the particle scattering phase functions and the gas vertical profiles that we used may be different from the actual profiles on Titan. It would modify the angular description of the modeled intensities and of the retrieved surface albedo. Therefore, it could induce another bias because the two images are not taken with the same observation geometry.

6.4. Water-ice distribution results

The maps of different non-normalized ratio values for both VIMS cubes are in Fig. 14, and the δ values are presented in Fig. 15. Given our estimated uncertainties, the extreme values of the

ratios (in red and blue) are significant. Furthermore, similar structures stand out on both cubes, although we cannot compare the absolute values as the illumination and viewing geometries are different between C15 and C18 that, in addition, were acquired 7 years apart. It is also important to remind that the ice crust on Titan is covered by sedimented aerosols (Janssen et al., 2016; Brossier et al., 2018). The sediment layer thickness has an influence on VIMS spectral channels ratios (Rannou et al., 2016). In both Fig. 14 and 15, units exhibiting different strength of the water ice signal according to the multi-criteria analysis of C18 (Fig. 15-d) are outlined. In C15, we do observe the highest water ice signature on Xanadu mountains, and a medium-high signature at 24° S 120° W, next to the dune unit. Surprisingly, in C18, the strongest signals are not in the same place as in C15. They are at the ends of the channels in blue dotted areas, which only displays a medium water ice signature in C15. There is a clear correlation between the structures on the RADAR map, and the signature of water ice. For example the blue dotted areas tend to correspond to dark and smooth gray structures in the lowest resolution part of the RADAR map. The area with low water-ice signature around 23.5° S 116° W corresponds to the dune unit in the RADAR map, and its surrounding dark gray halo. The halo has a lower water-ice signature than its center. A dark gray terrain at 22° S 122° W on the RADAR map is also well delimited by a low δ on C15, and a medium-low one in C18. This is also the case for the medium-low δ on the top corners of C18. The largest terrain with low δ is located in Tui Regio. Ratios are of medium value in the channel beds, suggesting a slightly higher water ice signature than in the surrounding terrains (see Fig. 14-d-e for the most flagrant). Even if the error on these regions reduces the significance of these variations, we do observe the same trend in both cubes. This support the hypothesis that the channels descend from the mountains, and contain water ice cobbles, probably covered by organic sediments. Above all, we notice the presence of an area of high δ at the end of each channel.

The color code in Fig. 13 is set to highlight in dark blue terrains with high water ice signature. However, our results (Fig. 14 and 15) reveal areas with strong water ice signal in dark brown for C15 (Fig. 13-a). For C18 the highest water ice signatures are in dark brown, and dark blue areas. This confirms the need of a radiative transfer analysis to extract the surface signal from the atmospheric signal, and to characterize the nuances of the water-ice signal intensity.

[[Image]]

Figure 14: Values of the ratios 2.7/2.8 (top panels), 2.0/1.28 (middle panels), and 1.59/1.28

(bottom panels) for the VIMS cubes C15 (a,c,e), and C18 (b,d,f) respectively, superimposed on the RADAR map. Each point corresponds to the position of a pixel of the cubes. Channels are outlined by purple lines, and areas of low and high water-ice signal are circled in yellow and blue, respectively. The absolute error for each ratio is: (a) ± 0.05, (b) ± 0.15, (c) ± 0.05, (d) ± 0.05, (e) ± 0.07, (f) ± 0.06.

[[Image]]

Figure 15: Values of the multi-criteria analysis parameter δ for the VIMS cubes C15 (a), and C18 (b) respectively, superimposed to the RADAR map. Each point corresponds to the position of a pixel from the cubes. Channels are outlined by purple lines. Regions of high and low δ are annotated in blue and yellow lines respectively, and fans highlighted by Radebaugh et al. (2018) are represented by green dots.

[[Image]]

Figure 16: I/F spectra of pixels (34,16) and (15,25) of the cube C18 with low (red) and high (blue) values of our water-ice signal criteria δ (top panel), and their respective albedo (bottom panel).

Fig. 16 displays the spectra and surface albedo of two pixels taken in zones of low and high water-ice signature for the cube C18 (respectively, $\delta = 0.5$, and $\delta = -3.4$). The presence of water-ice darkens the albedo in most of Titan's atmospheric windows (see Fig. 11 water-ice absorptions), consequently lowering the I/F, whereas where the water-ice signal is low, the albedo is increased. This effect is especially significant at 1.5, 2, 2.8 and 5 μm. However the shape of the albedo for the 2.8 μm window changes the most.

7. Discussion on the water ice signature and on geological structures

With the color maps, we can discuss the meaning of the ice index and the connection with surface features and processes. At first glance, the two dataset C15 and C18 yield, for each color ratios and for the multicriteria (δ), similar and consistent maps. However, we note that the

absolute values reported on the maps systematically differ between C15 and C18. We also remark that the nature of some areas clearly differs, which reveals changes between the two flybys. We describe in this section the factors that help understanding our maps and the parameters that could influence and modulate the retrieved surface albedos, ratios and multicriteria index in the maps.

7.1. Grain size and sediment cover

First of all, the intensity of water ice signatures depends on the size of ice grains. Data displayed in Fig. 11-b clearly illustrates this dependence. This stresses that a change in the strength of water ice signature could be due to a change in the average size of ice grains composing the uppermost layer of Titan's ground, or to a thicker sedimentary layer covering or mixed with the ice layer (Brossier et al., 2018). Based on this figure, the ratio $2.7/2.8$ could be (with caution) used as an indicator of the grain size due to the strong absorption of water ice at 2.9 to 3.25 μm. The higher the ratio is, the smaller the grain size is. It could be directly used to classify different terrains if the sedimentary layer is homogeneous. If the sedimentary layer is not homogeneous, disentangling the two effects is not possible because the effect of a coverage by sediments is not known. A specific model is needed to interpret the details of the color ratio in term of physical parameters, like what was done in Brossier et al. (2018), where they noted in the IR-blue terrains a grain size generally larger than 100 μm and half as many solutions with a grain size smaller than 0.1 μm. Another difficulty arises because the 2.7-2.8 μm window is incompletely treated with ethane and possibly other molecules absorptions missing in the model.

Therefore, in this work, we can compare and classify the different terrains with the color ratio and the multicriteria index. It means that we discuss the apparent presence of water ice, but we have to keep in mind that more or less prominent ice signature may have multiple origin and can not be directly linked to the real amount of ice at the surface.

Using a ratio instead of absolute band values allow us to still be more sensitive to water ice absorption. Fig. 14-a and -b show different patterns between C18 and C15. Similarity still arises: on both cubes, at the beginning of the channels, the $2.7/2.78$ ratio is lower than at the bottom. However the differences are within the estimated error bars. Taking this into account, as noted previously, there is either a variation of the grain size in the cube indicating a larger grain size in Xanadu, a variation of abundance of water ice, and/or a disparity in the dust layer thickness. In the case of sediment transport, smaller and lighter grains travel generally further as less energy is

required to move the particles (Gyr and Hoyer, 2006). We then expect larger grains on Xanadu at the channels origin, and that further along the river the grain size decreases, as inferred here.

7.2. Seasonal cycle and dust storm

As noted previously, we observe differences between C15 and C18, either for the haze and mist scale factors, or for δ. Surface albedo are retrieved with a specific setup of absorption and scattering properties in the atmosphere, given in detail in previous sections. But, this should be considered as an operational description, with some parameters determined by previous studies, predicted by models or set by free parameters. Constraining the atmosphere properties for retrieving the same surface albedo with C15 and C18 would be possible. However, the atmosphere characteristics (particle vertical and gas profiles, phase functions,...) may also change with time. The two observations were taken 7 years apart, over the north spring equinox. Some atmospheric properties probably have changed between these two dates, especially the haze and mist vertical profiles (Vinatier et al., 2010; Seignovert et al., 2020). This explains well why the amount of particles needed to fit data changes between these two dates. But, the actual change in haze and mist profiles can not be accounted in detail by simple parameters such as the haze and mist factors (F_h and F_m). The global shifts in color ratio and in the multicriteria index between the two observation sets can then be also explained by a real change in atmosphere properties.

The maps derived from observations also differs in some areas with obvious changes in water ice signatures compared to the surrounding. For instance, a strip of several pixels width at the northern edge of the maps retrieved with C15 systematically has a stronger ice signature than the pixels a bit south. This strip does not exist in C18. Notably, this strip corresponds to the southern edge of Xanadu mountains, delineated in Figure 1 and 15. These changes in color ratios and in δ indicate changes in the composition of the uppermost surface layer.

Two specific processes, which are not mutually exclusive, may explain these regional changes. First, the amount of deposited material rate of the aerosols is low on Titan, but dust storms probably occurred in between 2008 and 2010 due to the equinox (Charnay et al., 2015; Rodriguez et al., 2018), and one particularly at the East side of Xanadu. It could have influenced the amount of deposited material in this period, and the number of large particles in the lower atmosphere issued from surface erosion. Such an event may have deposited a sufficiently thick layer of particles to change the layer's color relative to the surrounding. Secondly, Turtle et al.

(2011) report an episode of heavy rain during the equinoctial period in 2010, in the equatorial region. This occurred at 20° S, but at an another longitude than our region of interest. The rain flooded a wide region and produced an obvious and persistent change in surface reflectivity. A similar or less intense flooding may have occurred elsewhere in the same period of time. Rodriguez et al. (2011) report a significant cloud coverage in the south tropical band between 2007 and 2010. They report a cloud event in 2008 above 120° W and 20° S, comparable in term of apparent area to the event reported by Turtle et al. (2011). Such an event can probably alter or remove light sedimentary layers, eventually ice gravels or small pebbles and change locally both surface reflectivity and color ratios. Our maps, indeed, clearly show that an event changed the surface characteristics of some area compared to their surrounding.

7.3. Dunes

The water-ice signature variations can help identifying geological structures, by the shapes and values of those variations. Based on morphological arguments, Lopes et al. (2019) classified the terrains in C15 and C18 as "plains", "hummocky" for Xanadu mountains, "dunes" for the yellowish structure (at the bottom of Fig. 15-a and annotated in Fig. 15-a), and "dry lakebed" (Moore and Howard, 2010) for the RADAR-gray structure at the bottom left of the dunes (around 25° S,118.5° W) located in Tui Regio. Hummocky terrains are expected to be areas where the icy crust of Titan is more exposed than elsewhere on Titan (i.e., covered by a thinner layer of organic material) (Janssen et al., 2016), which is supported by our results on Xanadu. The so-called "dune unit" (Fig. 15-a), on the contrary, should be poor in water ice. Yet, both the albedo (especially at 5 μm) and inferred delta parameter in this area suggest the presence of a water ice component. The SAR image does not resolve any individual dunes but there are most likely present at a scale smaller than the RADAR resolution here and with interdune corridors enriched in water ice (Barnes et al., 2008; Bonnefoy et al., 2016).

7.4. Precipitations and Alluvial fans

We find an accumulation of high water-ice signature at the end of the channels. With arguments based on radar-brightness, Le Gall et al. (2010) have suggested that the bed of these channels could be ice-rich. Unfortunately, they are too narrow to be characterized in detail at

VIMS resolution. Brossier et al. (2018) interpret 'IR-blue' VIMS patches like our region of interest as possible accumulated erosional products from the icebed, that cover the layer of organic materials, or eroded icy terrains where rainfall washed out the organic layer. The revealed ice-rich signature features could be alluvial fans where sediments have been transported and deposited from the mountains of Xanadu. Such alluvial fan results from the abrupt decrease of the terrain's slope, inducing a slower stream flow and sediments deposit in the plains. There are generally triangular-shaped, similar to the features discussed here, with coarse sediments close to the mouth of the stream and smaller ones further away. The channels that carry materials to the fans can be dry most of the time, as this is most likely the case here and in desert regions on Earth, and occasionally be fed occasionally by violent rainfalls or storms.

As discussed in a previous section, rain showers and cloud activity occur during equinox at these latitudes (Turtle et al., 2011; Rodriguez et al., 2011; Turtle et al., 2018). As further evidences, other VIMS cubes with lower pixel resolution from the flyby T44 show a large and discontinuous cloud, with an orientation W-E. Strikingly, Griffith et al. (2005) detected a rapid evolution of mid-latitude clouds, that eventually dissipated as a rain fall within a few hours. Such hydrologic events may be the source of liquid alimenting sporadically the channels considered here. A high discharge of liquid and a non-porous soil is needed to transport sediments over 300 km in a dry region. This aspect is also discussed by Faulk et al. (2017) and Birch et al. (2016), who have considered occasional intense rainfalls at 20° S of latitude, that can create alluvial fans.

The extrapolated topography from Corlies et al. (2017) does not show abrupt slope decrease at this particular site (maybe because of a low resolution), but Birch et al. (2016) do find equatorial fans in Xanadu region. However they do not classify these blue dotted areas as fans. Radebaugh et al. (2018) mention fans in our area of study (green dots in Fig. 1 and 15), but these patterns appear to be much smaller than what we observe. Although, when we look closely at our results in Fig. 15-b, we notice that in most cases the green dots' signature of water-ice is a bit higher than the area surrounding the dots. Another origin may also explains the presence of these enhanced water-ice signature at the foot of channels, between 17 and 19° S.

7.5. Impact craters

To investigate the nature of the spots of high water-ice signature, it may be relevant to put our zone of study in a broader context. Few craters impact exist on Titan, compared to other moons

(Wood et al., 2010; Neish et al., 2013). This feature can be explained by the presence of a dense atmosphere, and can be the consequence of and deposition by eolian and fluvial activities. Resurfacing by tectonic or cryovolcanism may also play a role. Impact craters on Titan, particularly if they are young, are windows to the crust and therefore have ice-rich inner and outer rim (Janssen et al., 2016; Griffith et al., 2019). Compared with the rest of Titan, their rims are radar-bright with low emissivity at 2.2cm, like that of the hummock terrains (Lopes et al., 2019). On Titan, low emissivity appears to be associated with water-ice (Malaska et al., 2016; Janssen et al., 2016).

Xanadu is a complex zone with multiple ancient impact crater candidates (Wood et al., 2010). The global mosaic map of VIMS-ISS (Seignovert et al., 2019) in Fig. 17-a, reveals 2 giant circular shapes on Xanadu (crater #1 and #2 in this Fig. 17). These features could be artifacts due to the enhanced resolution of VIMS dataset in these areas compared to the rest of Xanadu. However, crater #1 is also visible on the emissivity map (Fig. 17-b) as a large-scale low emissivity region. Brown et al. (2011) argue in favor of a giant crater called XCF. The spots of enhanced water-ice downstream are located at the limit of a circular feature that could correspond to the rim of crater #2 but there is no noticeable ring-like feature on the emissivity map, probably due to the low resolution of the bottom half part of the map for this potential crater. Instead, they could also correspond to the inner ring of crater #1. Finally, crater #4 may be the inner ring of crater #1.

Though, giant impacts are not required to create these putative rims. Smaller potential craters exist in Xanadu. They are numbered form 3 to 7 in our region of interest. We select potential craters when they check at least 2 of these following criteria: a circular shape in Fig. 17-c, a low emissivity spot on Fig. 17-b and a corresponding geological crater-like feature in Fig. 17-a. Putative craters #6 and #7 may be associated with water-ice enhanced signal on the rims. Putative craters #3, #4 and #5 are too far from the area of enhanced water ice signal, but it would be interesting to investigate those features in more details. Remarkably, high δ spots and channels often correspond to value of medium emissivity.

Despite these correlations, we do not find them convincing enough to ascertain that impact craters were the cause of the enhanced water-ice signatures at the channels' ends.

[[Image]]

Figure 17: (a) Zoom of Titan's ISS_VIMS map from Seignovert et al. (2019) on Xanadu

Journal Pre-proof

region,(b) Titan's 2.2cm wavelength emissivity map from Janssen et al. (2016), and (c) Titan RADAR map, with outlined potential crater areas. The dashed rectangle is our zone of study, and the thin black line represent the channels.

7.6. Delta and evaporites

MacKenzie and Barnes (2016) classify Tui Regio as an evaporitic terrain. This is in good agreement with our results showing a very low water-ice signature inside this area (i.e. the yellow dashed area in Fig. 15). This region is suspected to be a paleo sea (Moore and Howard, 2010; Hofgartner et al., 2020). While it is not incompatible with an old impact crater formation, as seas may form in craters, it casts a doubt on the origin of the water-ice signature enhancement at the border of Tui Regio, where the channels end. If the channels where active at the same time of the sea, these features could be delta-like formations, occurring when the stream is slowed down at the contact of the sea, resulting in an accumulation of fine deposits at the margins of Tui Regio. If these structures are deltas, it could imply that the channels supplied the paleo-sea. One ice-rich (high δ) area (130 ± 1° W,16 ± 1.5^{o} S) does not seem to end a channel, but it may be because it was too old or too narrow to be detected on the RADAR map. If precipitations are sufficient, rainstorms also could make small or subsidiary channels not resolved with the RADAR resolution overflows and deposit washed off sediments at the margins of the paleo-sea.

Another ice-rich area (119 ± 2° W, $24 \pm 1.^{o}$ S) seems to be connected to a remote channel through a broad and diffuse river bed, not different but much longer that the structures that connects the other channels to the ice-rich zones. This is a possible old channel, highlighted in Fig. 15 (in purple dotted line).

Our results also show a gradual increase of δ from the center towards the borders of Tui Regio. This result is consistent with the pattern predicted by Cordier et al. (2016), in their Fig. 10 showing a decrease of the evaporitic layer's thickness with the distance from the center of the sea. However VIMS only probes the surface firsts tens of microns, so if there is a thickness variation, it is on a micrometric scale. A more probable interpretation would be a change of composition in the evaporitic layer due to the different saturation values of the components in the liquid (Cordier et al., 2013, 2016).

North to the deltas, depending on the observation, color on Xanadu mountains are contrasted. In C15, Xanadu mountains appear with a high ice-index (forming the ice-rich strip

discussed previously). The plain at the foot of the mountains has a low ice signal and it is then probably covered by sediment. In C18, Xanadu mountains and the plains below appear to be quite uniform, regardless the topography. Differences between the two observations, as explained above, may be due to meteorological events or to the different incident and emergent angles if the surface reflectivity is not isotropic as assumed in our model.

The explanation of our ice index maps (ratios and δ) with dry (occasionnally active) river beds ending in delta formations at the edge of a paleolake appears the most consistent with observations. These rivers seem to flow from Xanadu mountain slopes. The site topology could have been formed by impact craters but they do not seems to be the direct reason for ice rich terrains to be apparent.

8. Conclusion

In this work we used a model of photometry to account for atmosphere scattering and absorption. The purpose is to retrieve the surface albedo and to remove as much as possible the effects due to the atmosphere and the observation geometries. The model setup is quite standard and derived from previous models (Rannou et al., 2010). Among other specific characteristics, we use a model of scattering by fractal aggregates (Rannou et al., 1997) to calculate the optical properties of the haze. Our simulations show the need for aerosols with a fractal dimension between 2.3 and 2.4, i.e., more compact than initially assumed (2.0). This is obviously meaningful in term of aerosol growth and in term of mechanical behavior in the atmosphere. This updated fractal dimension reduces and flattens the surface albedo spectra. It also changes its shape at 1.3 μm.

The haze opacity varies over large distances, and not always along the latitude. The mist opacity factor changes over shorter distances than the haze opacity factor, as expected since it is more sensitive to variations of the lower atmosphere. Our study confirms that these two factors are not correlated. Seasonal cycle may also increase the haze parameter, but further studies are required to confirm the influence of a seasonal cycle on the haze over several years.

The photometry model enabled us to retrieve the surface albedo in seven methane windows, and for the pixels of two VIMS cubes probing the region between Xanadu and Tui regio. This region is of some interest as it is assumed to be an ancient sea. We established several criteria to detect water ice signature (four ratios and a global index). The radiative transfer analysis

Journal Pre-proof

highlights areas of high water-ice signal on Xanadu mountains and also at the far end of dry channels. Areas shapes of high water-ice signal at the stream mouths are triangular as expected for alluvial fans, or deposits of deltas. In the first case an abrupt slope change is needed, and in the second case the channels supply the paleo-sea of Tui Regio. Impact craters with ice-rich rims is a less likely explication for these features. The ice signal decreases inside the channels, perhaps due to their sizes, smaller than the spatial resolution of a VIMS pixel. Anyhow, our results support Barnes et al. (2007), Langhans et al. (2012) and Brossier et al. (2018) hypothesis of sediment transport from Xanadu mountains to the channels downstream, with a decreasing grain size.

In addition, our analysis shows a gradient of low δ perfectly superposed to Tui Regio. This gradient could correspond to the decreasing thickness from the center to the border of the evaporite layer of Tui Regio, as suggested by Cordier et al. (2016) or a variation of composition in the evaporite layer. Here the overall shape of the albedo between a low and high δ does not really change, except at 2.8 μm, i.e., in a domain where the model is incomplete. Detailed analysis of the retrieved albedo could bring further insight into the spectral composition of these terrains provided the uncertainties are small enough. We used an original method to provide estimate of the VIMS instrument intrinsic noise. This latter tends to increase with the wavelength, with $\sim$ 1% at short wavelengths to 10-40% above 3.5 μm. The error also varies from one cube to another.

Comparing our results to previous global mapping and RGB composites (Fig. 2), we see that the link between water ice and 'dark blue', and 'bright blue' areas is not as straightforward as it was previously thought (Barnes et al., 2007). The ice signature can be modulated by grain size, dust cover that darkens the albedo, or even the incident angles. Indeed, a light blue area in Fig. 2 is actually associated with a low water ice signal in Fig. 15-a whereas some black units corresponds to high values of δ. Only the RT analysis shows qualitatively the difference in intensity of water-ice signature between those blue units.

A surface albedo map leads to a better understanding of the structures. It allows removal of the atmospheric inputs and to correct effects of different observation geometries - except for the surface photometric function since we model surface reflectivity as a lambertian surface. These effects can deeply alter the perception of the true surface features by inducing strong biases. The different albedo ratios and the parameter δ that we consider in this work also have a much better contrasts than a direct analysis of radiance at the top of the atmosphere. They give a direct appreciation of the strength of the water-ice signature. Nonetheless, we are conscious of the limits

of δ. Since it is calculated using normalized ratios, meaning that for a VIMS cube with absolutely no water-ice, δ could still reach 0.5. That is why we must use it in addition to other methods of surface analysis. The model can be improved to obtain identical absolute ratios for VIMS cubes in a similar area, at the same time period and under different geometries. This is possible, for example, with better aerosol phase functions and better information about the vertical profile of haze and mist. More study is required on the mist and haze to retrieve the absolute value of the contrasts observed as water-ice signature. If our model is not perfect, it shows a possible way to obtain more information about the surface in the future.

The terrains studied in this paper are of great interest in terms of exobiology. Similar terrains on Earth, with sediment accumulation areas (deltas, paleo-lakes) are places where bio-signatures are generally well preserved (Meyers and Teranes, 2002). It would be particularly relevant for *Dragonfly* to visit areas similar to the region studied in our work (Lorenz et al., 2018). The mission will target zones with ice-rich material, which will help alleviate the ambiguity of VIMS analysis by finding the composition of the famous 'dark material' often mixed with the ice (Barnes et al., 2020).

There are probably plenty of other areas like those identified but not resolved by VIMS: the images from the descent of *Huygens* actually suggest the existence of river networks that are undetectable by VIMS or the RADAR because of their small dimensions (Owen, 2005).

Lastly, the approach proposed here can be applied to other regions in order to study qualitatively the water-ice signature on Titan, like Shangri-La, future landing site of *Dragonfly* and where *Huygens* landed. The averred flooded area in Turtle et al. (2011) paper could also be of interest. The model needs no specific adaptation for equatorial or tropical regions, but probably moderate adaptation for mid-latitude regions (from $\pm$ 30° to 50°) because the haze layer still has a vertical profile similar to the equatorial one. On the other hand, to be able to study polar regions, we need to adapt the vertical profile of aerosols and mist, and likely their spectral behavior.

Acknowledgements

The present research was supported by the Programme National de Planétologie (PNP) of CNRS-INSU co-funded by CNES, and also supported by the French HPC Center ROMEO, the Région Grand-Est and the University of Reims Champagne-Ardenne. Many thanks to Jérémie

Burgalat for the IT help provided.

References

Annex, A.M., Pearson, B., Seignovert, B., Carcich, B.T., Eichhorn, H., Mapel, J.A., von Forstner, J.L.F., McAuliffe, J., del Rio, J.D., Berry, K.L., Aye, K.M., Stefko, M., de Val-Borro, M., Kulumani, S., ya Murakami, S., 2020. Spiceypy: a pythonic wrapper for the spice toolkit. Journal of Open Source Software 5, 2050. URL: https://doi.org/10.21105/joss.02050, doi: 10.21105/joss.02050.

Barnes, J., Turtle, E., Trainer, M., Lorenz, R., Murchie, S., MacKenzie, S., 2020. Dragonfly: Nasa's rotorcraft lander for saturn's moon titan, in: American Astronomical Society Meeting Abstracts# 236, pp. 221–05.

Barnes, J.W., Bow, J., Schwartz, J., Brown, R.H., Soderblom, J.M., Hayes, A.G., Vixie, G., Le Mouélic, S., Rodriguez, S., Sotin, C., Jaumann, R., Stephan, K., Soderblom, L.A., Clark, R.N., Buratti, B.J., Baines, K.H., Nicholson, P.D., 2011. Organic sedimentary deposits in Titan's dry lakebeds: Probable evaporite. Icarus 216, 136–140. doi: 10.1016/j.icarus.2011.08.022

Barnes, J.W., Brown, R.H., Soderblom, L., Buratti, B.J., Sotin, C., Rodriguez, S., Mouèlic], S.L., Baines, K.H., Clark, R., Nicholson, P., 2007. Global-scale surface spectral variations on titan seen from cassini/vims. Icarus 186, 242 – 258. URL: http://www.sciencedirect.com/science/article/pii/S001910350600306X, doi: https://doi.org/10.1016/j.icarus.2006.08.021.

Barnes, J.W., Brown, R.H., Soderblom, L., Sotin, C., Le Mouèlic, S., Rodriguez, S., Jaumann, R., Beyer, R.A., Buratti, B.J., Pitman, K., et al., 2008. Spectroscopy, morphometry, and photoclinometry of titan's dunefields from cassini/vims. Icarus 195, 400–414.

Barnes, J.W., Brown, R.H., Turtle, E.P., McEwen, A.S., Lorenz, R.D., Janssen, M., Schaller, E.L., Brown, M.E., Buratti, B.J., Sotin, C., Griffith, C., Clark, R., Perry, J., Fussner, S., Barbara, J., West, R., Elachi, C., Bouchez, A.H., Roe, H.G., Baines, K.H., Bellucci, G., Bibring, J.P., Capaccioni, F., Cerroni, P., Combes, M., Coradini, A., Cruikshank, D.P., Drossart, P., Formisano, V., Jaumann, R., Langevin, Y., Matson, D.L., McCord, T.B., Nicholson, P.D., Sicardy, B., 2005. A 5-Micron-Bright Spot on Titan: Evidence for Surface Diversity. Science 310, 92–95. doi: 10.1126/science.1117075.

Journal Pre-proof

Barnes, J.W., MacKenzie, S.M., Young, E.F., Trouille, L.E., Rodriguez, S., Cornet, T., Jackson, B.K., Ádámkovics, M., Sotin, C., Soderblom, J.M., 2018. Spherical radiative transfer in c++ (srtc++): A parallel monte carlo radiative transfer model for titan. The Astronomical Journal 155, 264. URL: https://doi.org/10.3847%2F1538-3881%2Faac2db doi: 10.3847/1538-3881/aac2db.

Barnes, J.W., Radebaugh, J., Brown, R.H., Wall, S., Soderblom, L., Lunine, J., Burr, D., Sotin, C., Le Mouélic, S., Rodriguez, S., Buratti, B.J., Clark, R., Baines, K.H., Jaumann, R., Nicholson, P.D., Kirk, R.L., Lopes, R., Lorenz, R.D., Mitchell, K., Wood, C.A., 2007. Near-infrared spectral mapping of Titan's mountains and channels. Journal of Geophysical Research (Planets) 112, E11006. doi: 10.1029/2007JE002932.

de Bergh, C., Courtin, R., Bézard, B., Coustenis, A., Lellouch, E., Hirtzig, M., Rannou, P., Drossart, P., Campargue, A., Kassi, S., Wang, L., Boudon, V., Nikitin, A., Tyuterev, V., 2012. Applications of a new set of methane line parameters to the modeling of titan's spectrum in the 1.58 μ m window. Planetary and Space Science 61, 85 – 98. URL: http://www.sciencedirect.com/science/article/pii/S0032063311001577, doi: https://doi.org/10.1016/j.pss.2011.05.003. surfaces, atmospheres and magnetospheres of the outer planets and their satellites and ring systems: Part VII.

Birch, S., Hayes, A., Howard, A., Moore, J., Radebaugh, J., 2016. Alluvial fan morphology, distribution and formation on titan. Icarus 270, 238 – 247. URL: http://www.sciencedirect.com/science/article/pii/S0019103516000798, doi: https://doi.org/10.1016/j.icarus.2016.02.013. titan's Surface and Atmosphere.

Bonnefoy, L.E., Hayes, A.G., Hayne, P.O., Malaska, M.J., Le Gall, A., Solomonidou, A., Lucas, A., 2016. Compositional and spatial variations in titan dune and interdune regions from cassini vims and radar. Icarus 270, 222 – 237. URL: http://www.sciencedirect.com/science/article/pii/S0019103515004194, doi: https://doi.org/10.1016/j.icarus.2015.09.014. titan's Surface and Atmosphere.

Botet, R., Rannou, P., Cabane, M., 1995. Sensitivity of some optical properties of fractals to the cut-off functions. Journal of Physics A: Mathematical and General 28, 297–316. URL:

Journal Pre-proof

https://doi.org/10.1088%2F0305-4470%2F28%2F2%2F008 doi: 10.1088/0305-4470/28/2/008.

Brossier, J., Rodriguez, S., Cornet, T., Lucas, A., Radebaugh, J., Maltagliati, L., Le Mouélic, S., Solomonidou, A., Coustenis, A., Hirtzig, M., et al., 2018. Geological evolution of titan's equatorial regions: possible nature and origin of the dune material. Journal of Geophysical Research: Planets 123, 1089–1112.

Brown, R.H., Baines, K.H., Bellucci, G., Bibring, J.P., Buratti, B.J., Capaccioni, F., Cerroni, P., Clark, R.N., Coradini, A., Cruikshank, D.P., Drossart, P., Formisano, V., Jaumann, R., Langevin, Y., Matson, D.L., McCord, T.B., Mennella, V., Miller, E., Nelson, R.M., Nicholson, P.D., Sicardy, B., Sotin, C., 2004. The Cassini Visual And Infrared Mapping Spectrometer (Vims) Investigation. ssr 115, 111–168. doi: 10.1007/s11214-004-1453-x.

Brown, R.H., Barnes, J.W., Melosh, H.J., 2011. On titan's xanadu region. Icarus 214, 556 – 560. URL: http://www.sciencedirect.com/science/article/pii/S0019103511001096, doi: https://doi.org/10.1016/j.icarus.2011.03.018.

Charnay, B., Barth, E., Rafkin, S., Narteau, C., Lebonnois, S., Rodriguez, S., Courrech du Pont, S., Lucas, A., 2015. Nature Geoscience.

Clark, R.N., Brown, R.H., Lytle, D.M., Hedman, M., 2018. The VIMS Wavelength and Radiometric Calibration 19. NASA Planetary Data System, The Planetary Atmospheres Node.

Cordier, D., Barnes, J.W., Ferreira, A.G., 2013. On the chemical composition of Titan's dry lakebed evaporites. Icarus 226, 1431–1437. URL: http://www.sciencedirect.com/science/article/pii/S0019103513003278, doi: 10.1016/j.icarus.2013.07.026.

Cordier, D., Cornet, T., Barnes, J.W., MacKenzie, S.M., Le Bahers, T., Nna Mvondo, D., Ferreira, A.G., 2016. Structure of titan's evaporites. Icarus 270, 41–56. doi: 10.1016/j.icarus.2015.12.034, arXiv:1512.07294.

Corlies, P., Hayes, A.G., Birch, S.P.D., Lorenz, R., Stiles, B.W., Kirk, R., Poggiali, V., Zebker, H., Iess, L., 2017. Titan's Topography and Shape at the End of the Cassini Mission. Geophys. Res. Lett. 44, 11. doi: 10.1002/2017GL075518.

Cours, T., Cordier, D., Seignovert, B., Maltagliati, L., Biennier, L., 2020. The 3.4 μm absorption in titan's stratosphere: Contribution of ethane, propane, butane and complex hydrogenated

organics. Icarus 339, 113571. URL: http://www.sciencedirect.com/science/article/pii/S0019103519303719, doi: https://doi.org/10.1016/j.icarus.2019.113571.

Doose, L.R., Karkoschka, E., Tomasko, M.G., Anderson, C.M., 2016. Vertical structure and optical properties of titan's aerosols from radiance measurements made inside and outside the atmosphere. Icarus 270, 355 – 375. URL: http://www.sciencedirect.com/science/article/pii/S0019103515004534, doi: https://doi.org/10.1016/j.icarus.2015.09.039. titan's Surface and Atmosphere.

Emde, C., Buras-Schnell, R., Kylling, A., Mayer, B., Gasteiger, J., Hamann, U., Kylling, J., Richter, B., Pause, C., Dowling, T., Bugliaro, L., 2016. The libradtran software package for radiative transfer calculations (version 2.0.1). Geoscientific Model Development 9, 1647–1672. URL: https://www.geosci-model-dev.net/9/1647/2016/, doi: 10.5194/gmd-9-1647-2016.

Evans, K.F., 2007. Shdomppda: A radiative transfer model for cloudy sky data assimilation. J. Atmos. Sci. 64, 3854–3864. doi: 10.1175/2006JAS2047.1.

Faulk, S.P., Mitchell, J.L., Moon, S., Lora, J.M., 2017. Regional patterns of extreme precipitation on Titan consistent with observed alluvial fan distribution. Nature Geoscience 10, 827–831. URL: http://www.nature.com/articles/ngeo3043, doi: 10.1038/ngeo3043.

Fulchignoni, M., Ferri, F., Angrilli, F., Ball, A.J., Bar-Nun, A., Barucci, M.A., Bettanini, C., Bianchini, G., Borucki, W., Colombatti, G., Coradini, M., Coustenis, A., Debei, S., Falkner, P., Fanti, G., Flamini, E., Gaborit, V., Grard, R., Hamelin, M., Harri, A.M., Hathi, B., Jernej, I., Leese, M.R., Lehto, A., Lion Stoppato, P.F., López-Moreno, J.J., Mäkinen, T., McDonnell, J.A.M., McKay, C.P., Molina-Cuberos, G., Neubauer, F.M., Pirronello, V., Rodrigo, R., Saggin, B., Schwingenschuh, K., Seiff, A., Simões, F., Svedhem, H., Tokano, T., Towner, M.C., Trautner, R., Withers, P., Zarnecki, J.C., 2005. In situ measurements of the physical characteristics of Titan's environment. Nature 438, 785–791. doi: 10.1038/nature04314.

Goody, R., West, R., Chen, L., Crisp, D., 1989. The Correlated-k Method for Radiation Calculations in Nonhomogeneous Atmosphere. J. Quant. Spectrosc. Radiat. Transfer 42,

Journal Pre-proof

539–550.

Griffith, C.A., Lora, J.M., Turner, J., Penteado, P.F., Brown, R.H., Tomasko, M.G., Doose, L., See, C., 2012. Possible tropical lakes on Titan from observations of dark terrain. Nature 486, 237–239. doi: 10.1038/nature11165.

Griffith, C.A., Penteado, P., Baines, K., Drossart, P., Barnes, J., Bellucci, G., Bibring, J., Brown, R., Buratti, B., Capaccioni, F., Cerroni, P., Clark, R., Combes, M., Coradini, A., Cruikshank, D., Formisano, V., Jaumann, R., Langevin, Y., Matson, D., McCord, T., Mennella, V., Nelson, R., Nicholson, P., Sicardy, B., Sotin, C., Soderblom, L.A., Kursinski, R., 2005. The Evolution of Titan's Mid-Latitude Clouds. Sci 310, 474–477. doi: 10.1126/science.1117702.

Griffith, C.A., Penteado, P.F., Turner, J.D., Neish, C.D., Mitri, G., Montiel, N.J., Schoenfeld, A., Lopes, R.M.C., 2019. A corridor of exposed ice-rich bedrock across Titan's tropical region. Nat. Astron., 343doi: 10.1038/s41550-019-0756-5.

Gyr, A., Hoyer, K., 2006. Sediment Transport. 1 ed., Springer Netherlands.

Hansen, J.E., Travis, L.D., 1974. Light scattering in planetary atmospheres. Space Science Reviews 16, 527–610. URL: https://doi.org/10.1007/BF00168069, doi: 10.1007/BF00168069.

Hofgartner, J.D., Hayes, A.G., Campbell, D.B., Lunine, J.I., Black, G.J., MacKenzie, S.M., Birch, S.P.D., Elachi, C., Kirk, R.D., Le Gall, A., Lorenz, R.D., Wall, S.D., 2020. The root of anomalously specular reflections from solid surfaces on Saturn's moon Titan. Nat. Commun. 11, 2829. doi: 10.1038/s41467-020-16663-1.

Janssen, M., Gall, A.L., Lopes, R., Lorenz, R., Malaska, M., Hayes, A., Neish, C., Solomonidou, A., Mitchell, K., Kedebaugh, J., Keihm, S., Choukroun, M., Leyrat, C., Encrenaz, P., Mastrogiuseppe, M., 2016. Titan's surface at 2.18-cm wavelength imaged by the cassini radar radiometer: Results and interpretations through the first ten years of observation. Icarus 270, 443 – 459. URL: http://www.sciencedirect.com/science/article/pii/S0019103515004327, doi: https://doi.org/10.1016/j.icarus.2015.09.027. titan's Surface and Atmosphere.

Karkoschka, E., 2016. Seasonal variation of Titan's haze at low and high altitudes from HST-STIS spectroscopy. Icarus 270, 339–354. doi: 10.1016/j.icarus.2015.07.007.

Karkoschka, E., Schröder, S.E., Tomasko, M.G., Keller, H.U., 2012. The reflectivity spectrum and

Journal Pre-proof

opposition effect of titan's surface observed by huygens' disr spectrometers. Planetary and Space Science 60, 342–355.

Kazeminejad, B., Atkinson, D.H., Lebreton, J.P., 2011. Titan's new pole: Implications for the huygens entry and descent trajectory and landing coordinates. Advances in Space Research 47, 1622 – 1632. URL: http://www.sciencedirect.com/science/article/pii/S0273117711000664, doi: https://doi.org/10.1016/j.asr.2011.01.019.

Lafferty, W.J., Solodov, A.M., Weber, A., Olson, W.B., Hartmann, J.M., 1996. Infrared collision-induced absorption by n2 near 4.3 μm for atmospheric applications: measurements and empiricalmodeling. Appl. Opt. 35, 5911–5917. URL: http://ao.osa.org/abstract.cfm?URI=ao-35-30-5911, doi: 10.1364/AO.35.005911.

Langhans, M.H., Jaumann, R., Stephan, K., Brown, R.H., Buratti, B.J., Clark, R.N., Baines, K.H., Nicholson, P.D., Lorenz, R.D., Soderblom, L.A., Soderblom, J.M., Sotin, C., Barnes, J.W., Nelson, R., 2012. Titan's fluvial valleys: Morphology, distribution, and spectral properties. Planet. Space Sci. 60, 34–51. doi: 10.1016/j.pss.2011.01.020.

Le Gall, A., Janssen, M.A., Paillou, P., Lorenz, R.D., Wall, S.D., the Cassini Radar Team, 2010. Radar-bright channels on Titan. Icarus 207, 948–958. doi: 10.1016/j.icarus.2009.12.027.

Le Mouélic, S., Cornet, T., Rodriguez, S., Sotin, C., Seignovert, B., Barnes, J.W., Brown, R.H., Baines, K.H., Buratti, B.J., Clark, R.N., Nicholson, P.D., Lasue, J., Pasek, V., Soderblom, J.M., 2019. The Cassini VIMS archive of Titan: From browse products to global infrared color maps. Icarus 319, 121–132. doi: 10.1016/j.icarus.2018.09.017, arXiv:1809.06545.

Lellouch, E., Coustenis, A., Sebag, B., Cuby, J.G., López-Valverde, M., Schmitt, B., Fouchet, T., Crovisier, J., 2003. Titan's 5-μm window: observations with the very large telescope. Icarus 162, 125 – 142. URL: http://www.sciencedirect.com/science/article/pii/S0019103502000799, doi: https://doi.org/10.1016/S0019-1035(02)00079-9.

Levenberg, K., 1944. A Method for the Solution of Certain Non-Linear Problems in Least Squares. Quarterly of Applied Mathematic 2, 164–168.

Journal Pre-proof

Lopes, R., Malaska, M., Schoenfeld, A., Solomonidou, A., Birch, S., Florence, M., Hayes, A., Williams, D., Radebaugh, J., Verlander, T., Turtle, E., Le Gall, A., Wall, S., 2019. A global geomorphologic map of saturn's moon titan. Nature Astronomy, 1–6doi: 10.1038/s41550-019-0917-6.

Lorenz, R.D., Turtle, E.P., Barnes, J.W.,, Trainer, M.G., Adams, D.S., Hibbard, K.E., Sheldon, C.Z., Zacny, K., Peplowski, P.N., Lawrence, D.J., Ravine, M.A., McGee, T.G., Sotzen, K.S., MacKenzie, S.M., Langelaan, J.W., Schmitz, S., Wolfarth, L.S., Bedini, P.D., 2018. Dragonfly: A Rotorcraft Lander Concept for Scientific Exploration at Titan. Technical Report 3. Johns Hopkins APL.

MacKenzie, S., Barnes, J., 2016. Compositional Similarities and Distinctions between Titan's Evaporitic Terrains. The Astrophysical Journal 821, 0. URL: http://arxiv.org/abs/1601.03364{%}0Ahttp://dx.doi.org/10.3847/0004-637X/821/1/17, doi: 10.3847/0004-637X/821/1/17, arXiv:1601.03364.

MacKenzie, S.M., Barnes, J.W., Sotin, C., Soderblom, J.M., Le Mouélic, S., Rodriguez, S., Baines, K.H., Buratti, B.J., Clark, R.N., Nicholson, P.D., McCord, T.B., 2014. Evidence of Titan's climate history from evaporite distribution. Icarus 243, 191–207. doi: 10.1016/j.icarus.2014.08.022, arXiv:1408.2899.

Malaska, M.J., Lopes, R.M., Williams, D.A., Neish, C.D., Solomonidou, A., Soderblom, J.M., Schoenfeld, A.M., Birch, S.P., Hayes, A.G., Gall, A.L., Janssen, M.A., Farr, T.G., Lorenz, R.D., Radebaugh, J., Turtle, E.P., 2016. Geomorphological map of the afekan crater region, titan: Terrain relationships in the equatorial and mid-latitude regions. Icarus 270, 130 – 161. URL: http://www.sciencedirect.com/science/article/pii/S0019103516000889, doi: https://doi.org/10.1016/j.icarus.2016.02.021. titan's Surface and Atmosphere.

Maltagliati, L., Bézard, B., Vinatier, S., Hedman, M.M., Lellouch, E., Nicholson, P.D., Sotin, C., [de Kok], R.J., Sicardy, B., 2015. Titan's atmosphere as observed by cassini/vims solar occultations: Ch4, co and evidence for c2h6 absorption. Icarus 248, 1 – 24. URL: http://www.sciencedirect.com/science/article/pii/S0019103514005399, doi: https://doi.org/10.1016/j.icarus.2014.10.004.

Journal Pre-proof

Marquardt, D., 1963. An Algorithm for Least-Squares Estimation of Nonlinear Parameters. SIAM Journal on Applied Mathematics 11, 431–441. doi: 10.1137/0111030.

Mayer, B., Kylling, A., 2005. Technical note: The libRadtran software package for radiative transfer calculations ? description and examples of use. Atmospheric Chemistry and Physics Discussions 5, 1319–1381. URL: https://hal.archives-ouvertes.fr/hal-00303886.

McCord, T.B., Hansen, G.B., Buratti, B.J., Clark, R.N., Cruikshank, D.P., D'Aversa, E., Griffith, C.A., Baines, E.K.H., Brown, R.H., Dalle Ore, C.M., Filacchione, G., Formisano, V., Hibbitts, C.A., Jaumann, R., Lunine, J.I., Nelson, R.M., Sotin, C., the Cassini VIMS Team, 2006. Composition of Titan's surface from Cassini VIMS. Planet. Space Sci. 54, 1524–1539. doi: 10.1016/j.pss.2006.06.007.

McKay, C.P., Pollack, J.B., Courtin, R., 1989. The thermal structure of Titan's atmosphere. Icarus 80, 23–53. doi: 10.1016/0019-1035(89)90160-7.

McKellar, A., 1989. Low-temperature infrared absorption of gaseous n2 and n2 + h2 in the 2.0–2.5 μm region: Application to the atmospheres of titan and triton. Icarus 80, 361 – 369. URL: http://www.sciencedirect.com/science/article/pii/0019103589901462, doi: https://doi.org/10.1016/0019-1035(89)90146-2.

Meyers, P.A., Teranes, J.L., 2002. Sediment organic matter, in: Tracking environmental change using lake sediments. Springer, pp. 239–269.

Moore, J.M., Howard, A.D., 2010. Are the basins of titan's hotei regio and tui regio sites of former low latitude seas? Geophysical Research Letters 37. URL: https://agupubs.onlinelibrary.wiley.com/doi/abs/10.1029/2010GL045234, doi: 10.1029/2010GL045234, arXiv:https://agupubs.onlinelibrary.wiley.com/doi/pdf/10.1029/2010GL045234.

Moré, J.J., Garbow, B.S., Hillstrom, K.E., 1980. User Guide for MINPACK-1. Technical Report ANL-80-74. pub-ANL. pub-ANL:adr.

Neish, C.D., Kirk, R.L., Lorenz, R.D., Bray, V.J., Schenk, P., Stiles, B.W., Turtle, E., Mitchell, K., Hayes, A., 2013. Crater topography on Titan: Implications for landscape evolution. Icarus 223, 82–90. URL: http://dx.doi.org/10.1016/j.icarus.2012.11.030, doi: 10.1016/j.icarus.2012.11.030.

Journal Pre-proof

Nicholson, P.D., Ansty, T., Hedman, M.M., Creel, D., Ahlers, J., Harbison, R.A., Brown, R.H., Clark, R.N., Baines, K.H., Buratti, B.J., Sotin, C., Badman, S.V., 2020. Occultation observations of saturn's rings with cassini vims. Icarus 344, 113356. URL: http://www.sciencedirect.com/science/article/pii/S0019103518307334, doi: https://doi.org/10.1016/j.icarus.2019.06.017. cassini Mission Science Results.

Niemann, H.B., Atreya, S.K., Bauer, S.J., Carignan, G.R., Demick, J.E., Frost, R.L., Gautier, D., Haberman, J.A., Harpold, D.N., Hunten, D.M., Israel, G., Lunine, J.I., Kasprzak, W.T., Owen, T.C., Paulkovich, M., Raulin, F., Raaen, E., Way, S.H., 2005. The abundances of constituents of Titan's atmosphere from the GCMS instrument on the Huygens probe. Nature 438, 779–784. doi: 10.1038/nature04122.

Niemann, H.B., Atreya, S.K., Demick, J.E., Gautier, D., Haberman, J.A., Harpold, D.N., Kasprzak, W.T., Lunine, J.I., Owen, T.C., Raulin, F., 2010. Composition of Titan's lower atmosphere and simple surface volatiles as measured by the Cassini-Huygens probe gas chromatograph mass spectrometer experiment. J. Geophys. Res. 115, E12006. doi: 10.1029/2010JE003659.

Nixon, C.A., Temelso, B., Vinatier, S., Teanby, N.A., Bézard, B., Achterberg, R.K., Mandt, K.E., Sherrill, C.D., Irwin, P.G.J., Jennings, D.E., Romani, P.N., Coustenis, A., Flasar, F.M., 2012. ISOTOPIC RATIOS IN TITAN'S METHANE: MEASUREMENTS AND MODELING. The Astrophysical Journal 749, 159. URL: https://doi.org/10.1088%2F0004-637x%2F749%2F2%2F159 doi: 10.1088/0004-637x/749/2/159.

Owen, T., 2005. Huygens rediscovers titan. Nature 438, 756–757.

Radebaugh, J., Ventra, D., Lorenz, R.D., Farr, T., Kirk, R., Hayes, A., Malaska, M.J., Birch, S., Liu, Z.Y.C., Lunine, J., et al., 2018. Alluvial and fluvial fans on saturn's moon titan reveal processes, materials and regional geology. Geological Society, London, Special Publications 440, 281–305.

Rannou, P., Cabane, M., Botet, R., Chassefière, E., 1997. A new interpretation of scattered light measurements at titan's limb. Journal of Geophysical Research: Planets 102, 10997–11013. URL: https://agupubs.onlinelibrary.wiley.com/doi/abs/10.1029/97JE00

719, doi: 10.1029/97JE00719, arXiv:https://agupubs.onlinelibrary.wiley.com/doi/pdf/10.1029/97JE00719.

Rannou, P., Cours, T., Le Mouélic, S., Rodriguez, S., Sotin, C., Drossart, P., Brown, R., 2010. Titan haze distribution and optical properties retrieved from recent observations. Icarus 208, 850–867. doi: 10.1016/j.icarus.2010.03.016.

Rannou, P., Hourdin, F., McKay, C.P., Luz, D., 2004. A coupled dynamics-microphysics model of Titan's atmosphere. Icarus 170, 443–462. doi: 10.1016/j.icarus.2004.03.007.

Rannou, P., Toledo, D., Lavvas, P., D'Aversa, E., Moriconi, M.L., Adriani, A., Le Mouélic, S., Sotin, C., Brown, R., 2016. Titan's surface spectra at the Huygens landing site and Shangri-La. Icarus 270, 291–306. doi: 10.1016/j.icarus.2015.09.016.

Rey, M., Nikitin, A.V., Bézard, B., Rannou, P., Coustenis, A., Tyuterev, V.G., 2018. New accurate theoretical line lists of $^{12}CH_4$ and $^{13}CH_4$ in the $0-13400$ cm^{-1} range: Application to the modeling of methane absorption in Titan's atmosphere. Icarus 303, 114–130.

Rey, M., Nikitin, A.V., Tyuterev, V., 2016. TheoReTS – An information system for theoretical spectra based on variational predictions from molecular potential energy and dipole moment surfaces. J. Mol. Spectrosc. 327, 138–158.

Rey, M., Nikitin, A.V., Tyuterev, V.G., 2017. Accurate Theoretical Methane Line Lists in the Infrared up to 3000 K and Quasi-continuum Absorption/Emission Modeling for Astrophysical Applications. ApJ 847, aa8909.

Robidel, R., Mouélic], S.L., Tobie, G., Massé, M., Seignovert, B., Sotin, C., Rodriguez, S., 2020. Photometrically-corrected global infrared mosaics of enceladus: New implications for its spectral diversity and geological activity. Icarus 349, 113848. URL: http://www.sciencedirect.com/science/article/pii/S0019103520302293, doi: https://doi.org/10.1016/j.icarus.2020.113848.

Rodriguez, S., Le Mouélic, S., Barnes, J.W., Kok, J.F., Rafkin, S.C., Lorenz, R.D., Charnay, B., Radebaugh, J., Narteau, C., Cornet, T., Bourgeois, O., Lucas, A., Rannou, P., Griffith, C.A., Coustenis, A., Appéré, T., Hirtzig, M., Sotin, C., Soderblom, J.M., Brown, R.H., Bow, J., Vixie, G., Maltagliati, L., Courrech du Pont, S., Jaumann, R., Stephan, K., Baines, K.H., Buratti, B.J., Clark, R.N., Nicholson, P.D., 2018. Observational evidence for active dust storms on Titan at equinox. Nature Geoscience 11, 727–732. doi:

Journal Pre-proof

10.1038/s41561-018-0233-2.

Rodriguez, S., Le Mouélic, S., Sotin, C., Clénet, H., Clark, R., Buratti, B., Brown, R.H., McCord, T., Nicholson, P., Baines, K., et al., 2006. Cassini/vims hyperspectral observations of the huygens landing site on titan. Planetary and Space Science 54, 1510–1523.

Rodriguez, S., Le Mouélic, S., Rannou, P., Sotin, C., Brown, R., Barnes, J., Griffith, C., Burgalat, J., Baines, K., Buratti, B., Clark, R., Nicholson, P., 2011. Titan's cloud seasonal activity from winter to spring with cassini/vims. Icarus 216, 89 – 110. URL: http://www.sciencedirect.com/science/article/pii/S0019103511003034, doi: https://doi.org/10.1016/j.icarus.2011.07.031.

Rothman, L.S., Gordon, I.E., Babikov, Y., Barbe, A., Chris Benner, D., Bernath, P.F., Birk, M., Bizzocchi, L., Boudon, V., Brown, L.R., Campargue, A., Chance, K., Cohen, E.A., Coudert, L.H., Devi, V.M., Drouin, B.J., Fayt, A., Flaud, J.M., Gamache, R.R., Harrison, J.J., Hartmann, J.M., Hill, C., Hodges, J.T., Jacquemart, D., Jolly, A., Lamouroux, J., Le Roy, R.J., Li, G., Long, D.A., Lyulin, O.M., Mackie, C.J., Massie, S.T., Mikhailenko, S., Müller, H.S.P., Naumenko, O.V., Nikitin, A.V., Orphal, J., Perevalov, V., Perrin, A., Polovtseva, E.R., Richard, C., Smith, M.A.H., Starikova, E., Sung, K., Tashkun, S., Tennyson, J., Toon, G.C., Tyuterev, V.G., Wagner, G., 2013. The HITRAN2012 molecular spectroscopic database. J. Quant. Spectrosc. Radiat. Transfer 130, 4–50. doi: 10.1016/j.jqsrt.2013.07.002.

Schröder, S.E., Keller, H.U., 2006. The reflectance spectrum of Titan's surface at the Huygens landing site determined by the descent imager/spectral radiometer. Planet. Space Sci. 56, 753–769. doi: 10.1016/j.pss.2007.10.011.

Seignovert, B., Le Mouélic, S., Brown, R.H., Karkoschka, E., Pasek, V., Sotin, C., Turtle, E.P., 2019. Titan's global map combining vims and iss mosaics. URL: https://data.caltech.edu/records/1173, doi: 10.22002/D1.1173.

Seignovert, B., Rannou, P., 2019. Povray model of fractal aerosols. URL: https://doi.org/10.5281/zenodo.2559546, doi: 10.5281/zenodo.2559546.

Seignovert, B., Rannou, P., West, R.A., Vinatier, S., 2020. Haze seasonal variations of Titan's upper atmosphere during the Cassini Mission. Icarus In revision.

Soderblom, L.A., Kirk, R.L., Lunine, J.I., Anderson, J.A., Baines, K.H., Barnes, J.W., Barrett, J.M., Brown, R.H., Buratti, B.J., Clark, R.N., Cruikshank, D.P., Elachi, C., Janssen, M.A.,

Journal Pre-proof

Jaumann, R., Karkoschka, E., Mouélic, S.L., Lopes, R.M., Lorenz, R.D., McCord, T.B., Nicholson, P.D., Radebaugh, J., Rizk, B., Sotin, C., Stofan, E.R., Sucharski, T.L., Tomasko, M.G., Wall, S.D., 2007. Correlations between cassini vims spectra and radar sar images: Implications for titan's surface composition and the character of the huygens probe landing site. Planetary and Space Science 55, 2025 – 2036. URL: http://www.sciencedirect.com/science/article/pii/S0032063307001304, doi: https://doi.org/10.1016/j.pss.2007.04.014. titan as seen from Huygens.

Sotin, C., Jaumann, R., Buratti, B.J., Brown, R.H., Clark, R.N., Soderblom, L.A., Baines, K.H., Bellucci, G., Bibring, J.P., Capaccioni, F., Cerroni, P., Combes, M., Coradini, A., Cruikshank, D.P., Drossart, P., Formisano, V., Langevin, Y., Matson, D.L., McCord, T.B., Nelson, R.M., Nicholson, P.D., Sicardy, B., Le Mouelic, S., Rodriguez, S., Stephan, K., Scholz, C.K., 2005. Release of volatiles from a possible cryovolcano from near-infrared imaging of Titan. Nature 435, 786–789. doi: 10.1038/nature03596

Sromovsky, L., Fry, P., 2010. The source of widespread 3-μm absorption in jupiter's clouds: Constraints from 2000 cassini vims observations. Icarus 210, 230–257. doi: 10.1016/j.icarus.2010.06.039.

Stofan, E.R., Elachi, C., Lunine, J.I., Lorenz, R.D., Stiles, B., Mitchell, K.L., Ostro, S., Soderblom, L., Wood, C., Zebker, H., Wall, S., Janssen, M., Kirk, R., Lopes, R., Paganelli, F., Radebaugh, J., Wye, L., Anderson, Y., Allison, M., Boehmer, R., Callahan, P., Encrenaz, P., Flamini, E., Francescetti, G., Gim, Y., Hamilton, G., Hensley, S., Johnson, W.T.K., Kelleher, K., Muhleman, D., Paillou, P., Picardi, G., Posa, F., Roth, L., Seu, R., Shaffer, S., Vetrella, S., West, R., 2007. The lakes of Titan. Nature 445, 61–64. doi: 10.1038/nature05438.

Tomasko, M.G., Doose, L., Engel, S., Dafoe, L.E., West, R., Lemmon, M., Karkoschka, E., See, C., 2008. A model of Titan's aerosols based on measurements made inside the atmosphere. Planet. Space Sci. 56, 669–707. doi: 10.1016/j.pss.2007.11.019.

Turtle, E., Perry, J., Barbara, J., Del Genio, A., Rodriguez, S., Le Mouélic, S., Sotin, C., Lora, J., Faulk, S., Corlies, P., et al., 2018. Titan's meteorology over the cassini mission: Evidence for extensive subsurface methane reservoirs. Geophysical Research Letters 45, 5320–5328.

Turtle, E.P., Perry, J.E., Hayes, A.G., Lorenz, R.D., Barnes, J.W., McEwen, A.S., West, R.A., Del Genio, A.D., Barbara, J.M., Lunine, J.I., Schaller, E.L., Ray, T.L., Lopes, R.M.C., Stofan,

Journal Pre-proof

E.R., 2011. Rapid and Extensive Surface Changes Near Titan's Equator: Evidence of April Showers. Sci 331, 1414–1417. doi: 10.1126/science.1201063.

Turtle, E.P., Perry, J.E., McEwen, A.S., Del Genio, A.D., Barbara, J., West, R.A., Dawson, D.D., Porco, C.C., 2009. Cassini imaging of Titan's high-latitude lakes, clouds, and south-polar surface changes. Geophys. Res. Lett. 36, 2204. doi: 10.1029/2008GL036186.

Vinatier, S., Bézard, B., Lebonnois, S., Teanby, N.A., Achterberg, R.K., Gorius, N., Mamoutkine, A., Guandique, E., Jolly, A., Jennings, D.E., Flasar, F.M., 2015. Seasonal variations in Titan's middle atmosphere during the northern spring derived from Cassini/CIRS observations. Icarus 250, 95–115. doi: 10.1016/j.icarus.2014.11.019.

Vinatier, S., Bézard, B., Nixon, C.A., Mamoutkine, A., Carlson, R.C., Jennings, D.E., Guandique, E.A., Teanby, N.A., Bjoraker, G.L., Michael Flasar, F., Kunde, V.G., 2010. Analysis of Cassini/CIRS limb spectra of Titan acquired during the nominal mission. I. Hydrocarbons, nitriles and CO_2 vertical mixing ratio profiles. Icarus 205, 559–570. doi: 10.1016/j.icarus.2009.08.013.

Wood, C.A., Lorenz, R., Kirk, R., Lopes, R., Mitchell, K., Stofan, E., 2010. Impact craters on Titan. Icarus 206, 334–344. URL: http://dx.doi.org/10.1016/j.icarus.2009.08.021, doi: 10.1016/j.icarus.2009.08.021.

Journal Pre-proof

Highlights

- Strong water-ice signature on Titan's river deltas in South Xanadu.
- Fractal dimension of Titan's aerosols updated to 2.3.
- VIMS instrument error increases with wavelength.
- Possible chemical or thickness variation of evaporite layer in Tui Regio, Titan.

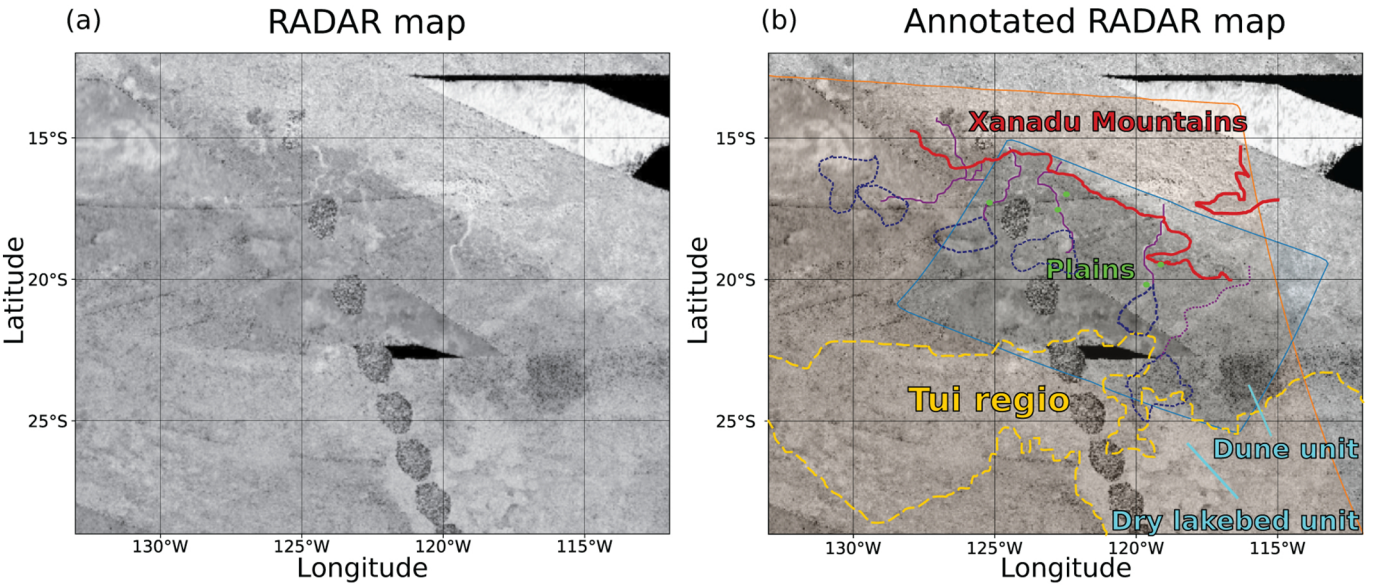
(a)
RADAR map
15°S
20°S
25°S
Latitude
130°W
125°W
120°W
115°W
Longitude
(b)
Annotated RADAR map
Xanadu Mountains
Plains
Tui regio
Dune unit
Dry lakebed unit
15°S
20°S
25°S
Latitude
130°W
125°W
120°W
115°W
Longitude

Figure 1

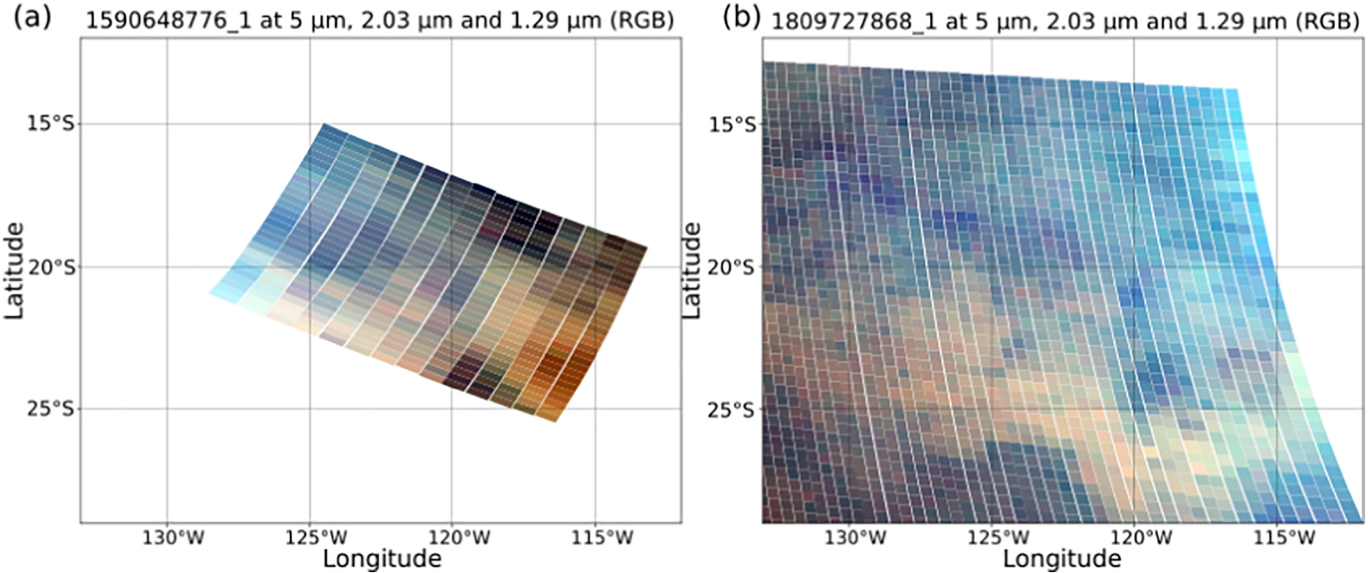
(a)
1590648776_1 at 5 µm, 2.03 µm and 1.29 µm (RGB)
15°S
20°S
25°S
Latitude
130°W
125°W
120°W
115°W
Longitude
(b)
1809727868_1 at 5 µm, 2.03 µm and 1.29 µm (RGB)
15°S
20°S
25°S
Latitude
130°W
125°W
120°W
115°W
Longitude

Figure 2

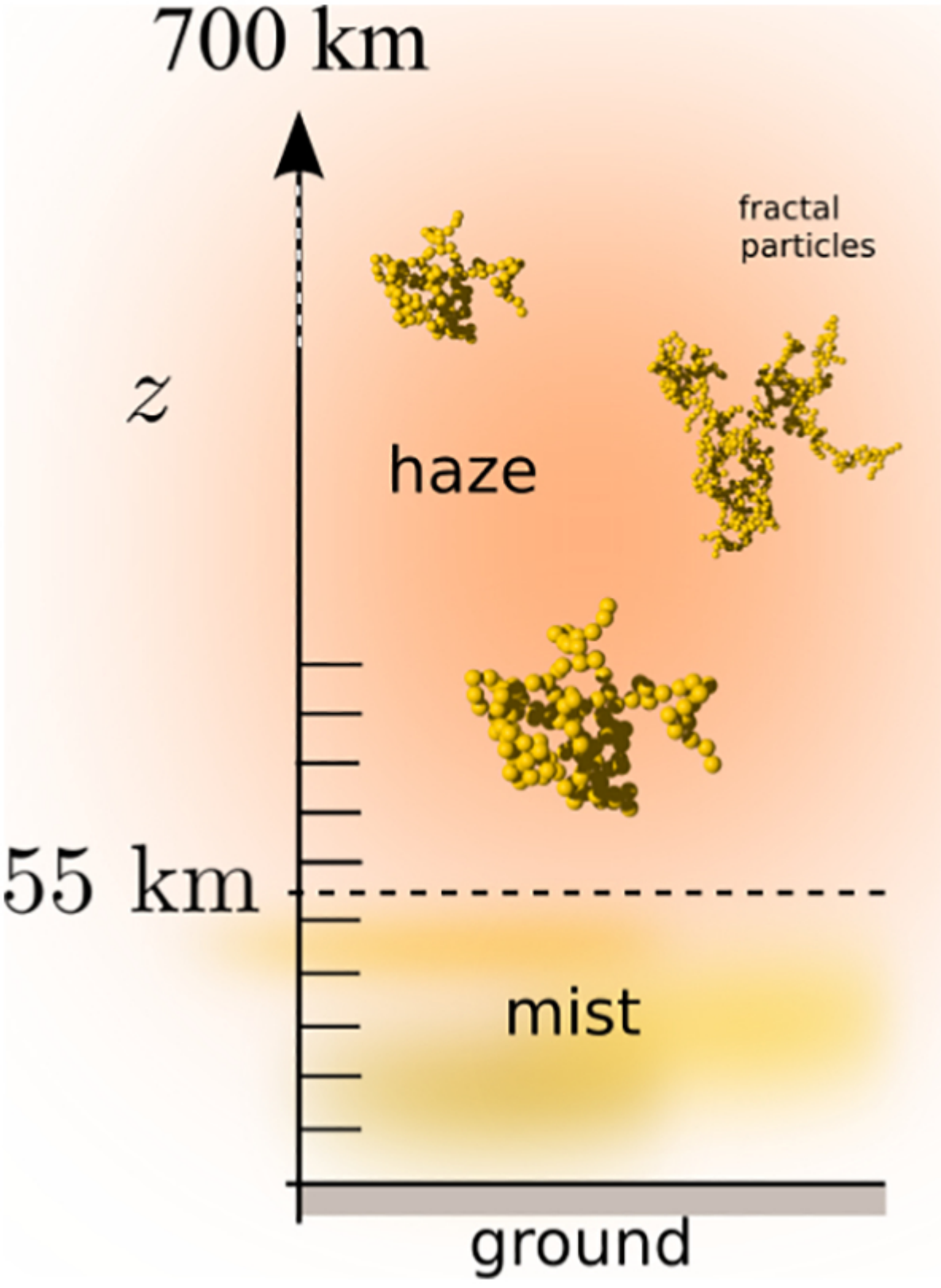

Figure 3

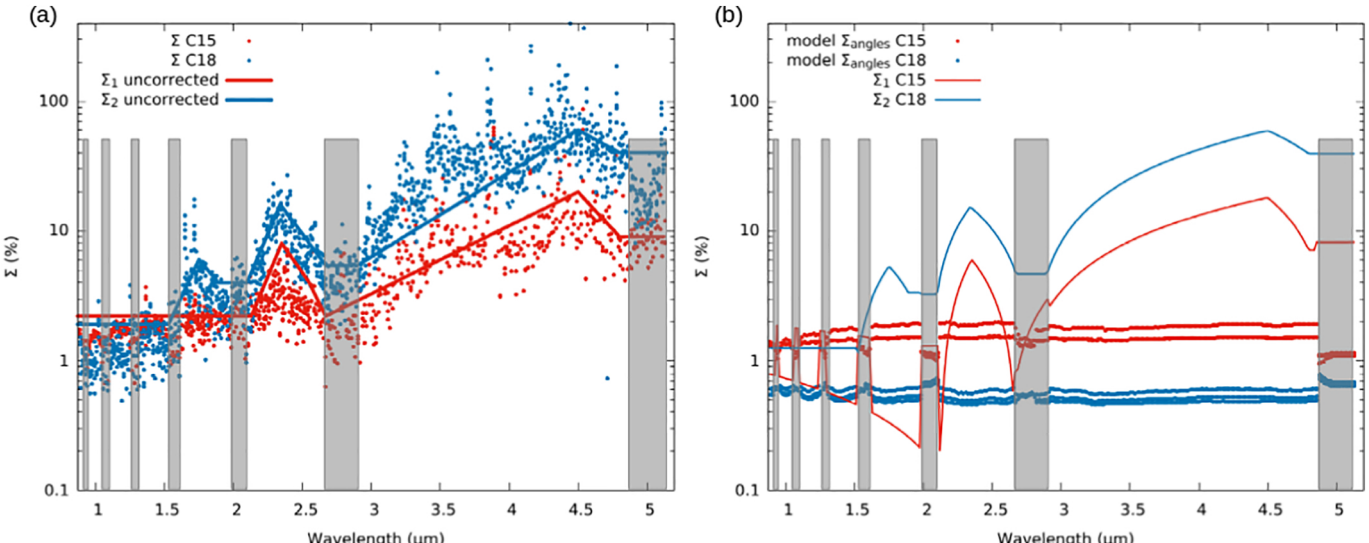
(a)
Σ C15
Σ C18
Σ1 uncorrected
Σ2 uncorrected
Σ (%)
Wavelength (μm)
(b)
model Σangles C15
model Σangles C18
Σ1 C15
Σ2 C18
Σ (%)
Wavelength (μm)

Figure 4

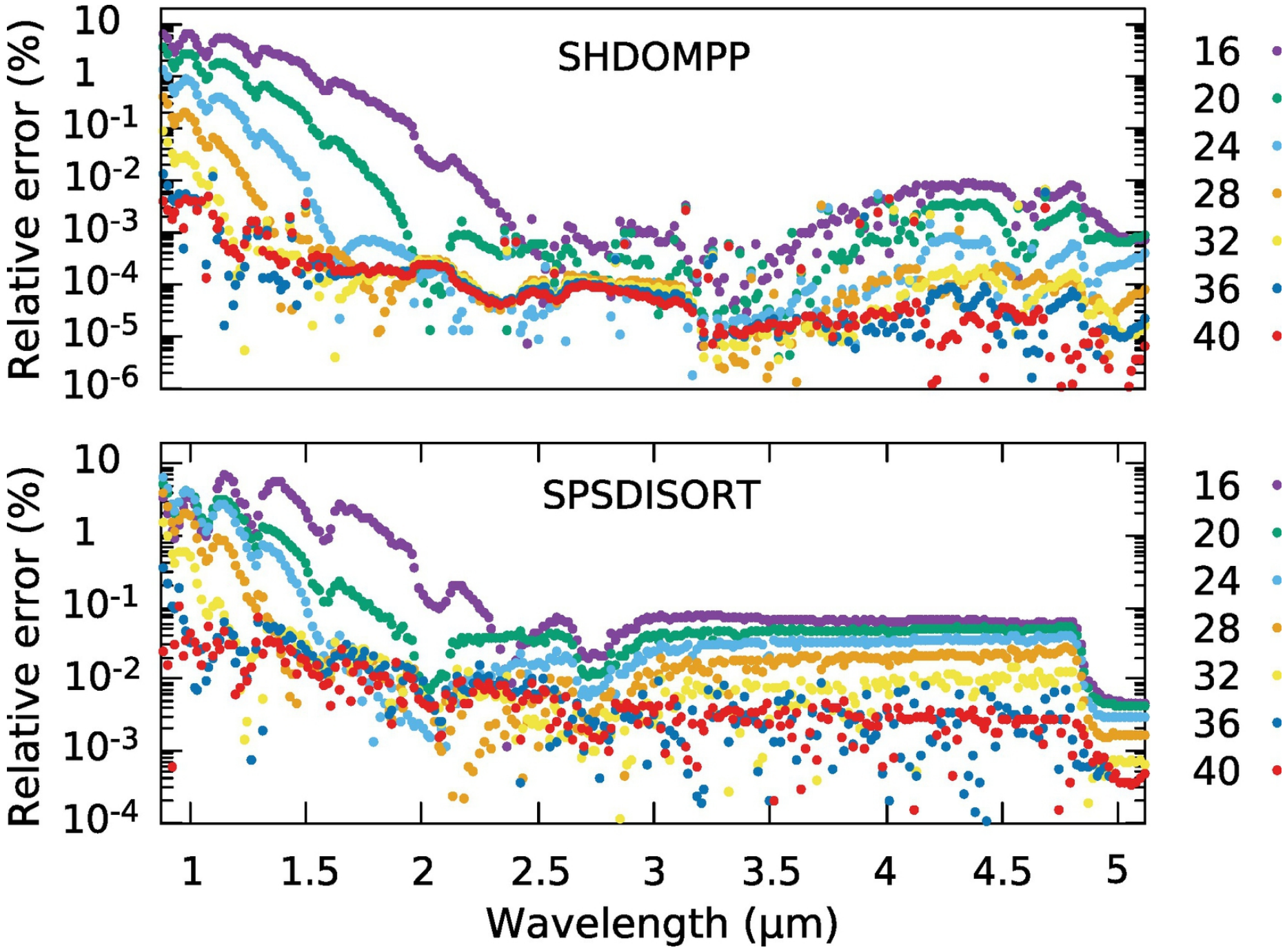
SHDOMPP
SPSDISORT
Relative error (%)
10
1
10-1
10-2
10-3
10-4
10-5
10-6
16
20
24
28
32
36
40
1
1.5
2
2.5
3
3.5
4
4.5
5
Wavelength (μm)

Figure 5

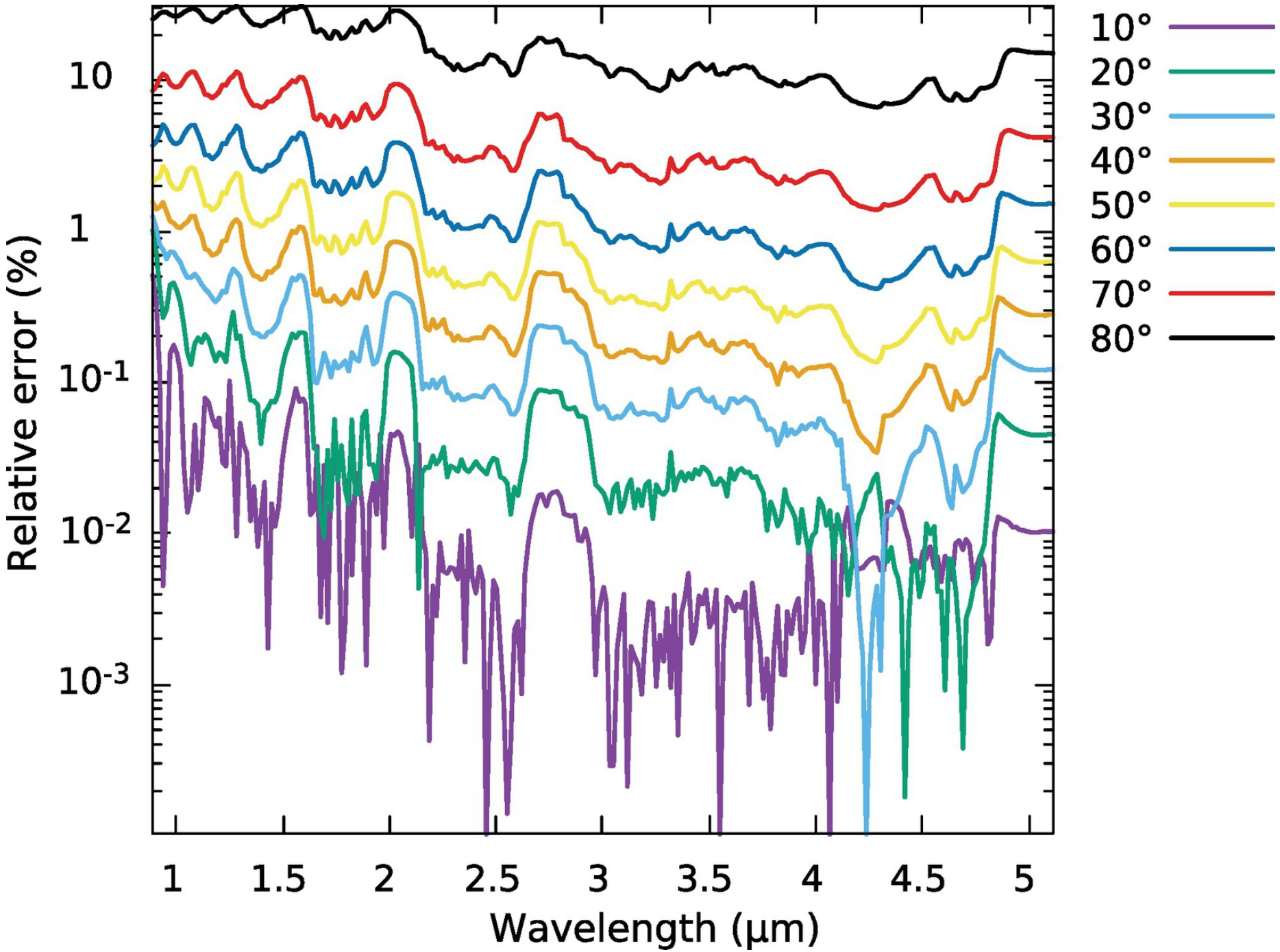
10°
20°
30°
40°
50°
60°
70°
80°
10
1
10-1
10-2
10-3
Relative error (%)
1
1.5
2
2.5
3
3.5
4
4.5
5
Wavelength (µm)

Figure 6

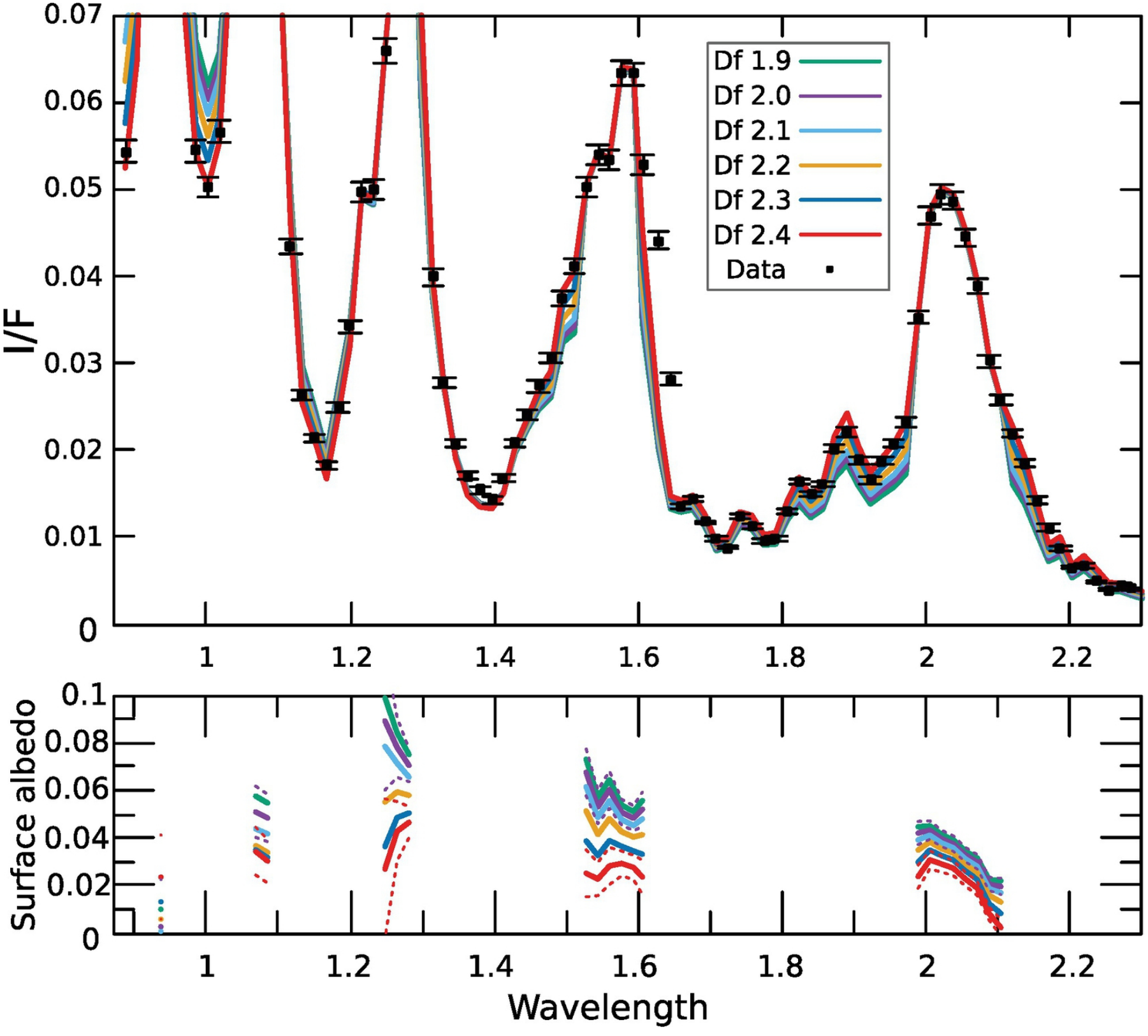
Df 1.9
Df 2.0
Df 2.1
Df 2.2
Df 2.3
Df 2.4
Data
I/F
0.07
0.06
0.05
0.04
0.03
0.02
0.01
0
1
1.2
1.4
1.6
1.8
2
2.2
Surface albedo
0.1
0.08
0.06
0.04
0.02
0
Wavelength

Figure 7

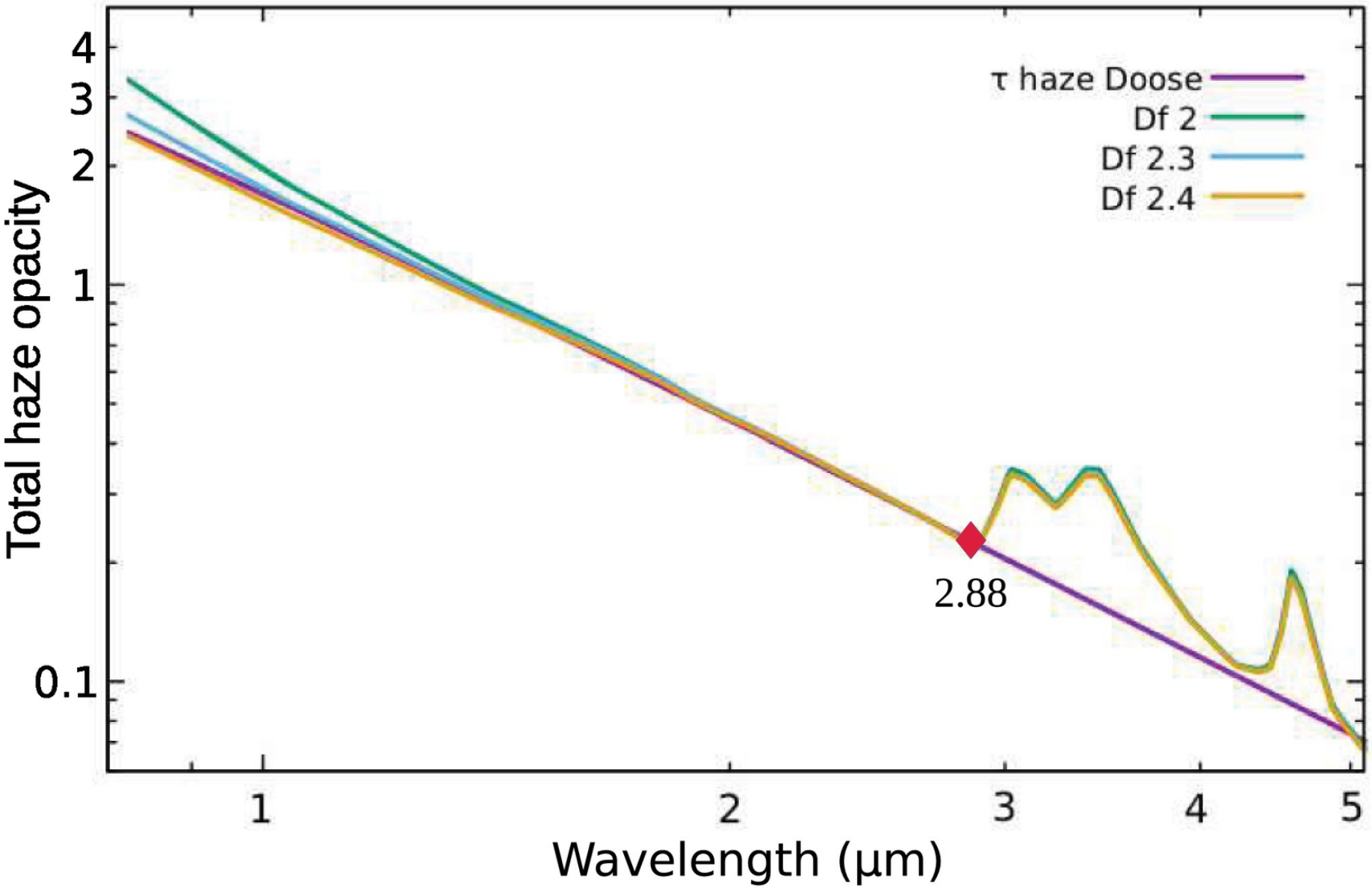
τ haze Doose
Df 2
Df 2.3
Df 2.4
Total haze opacity
4
3
2
1
0.1
2.88
1
2
3
4
5
Wavelength (μm)

Figure 8

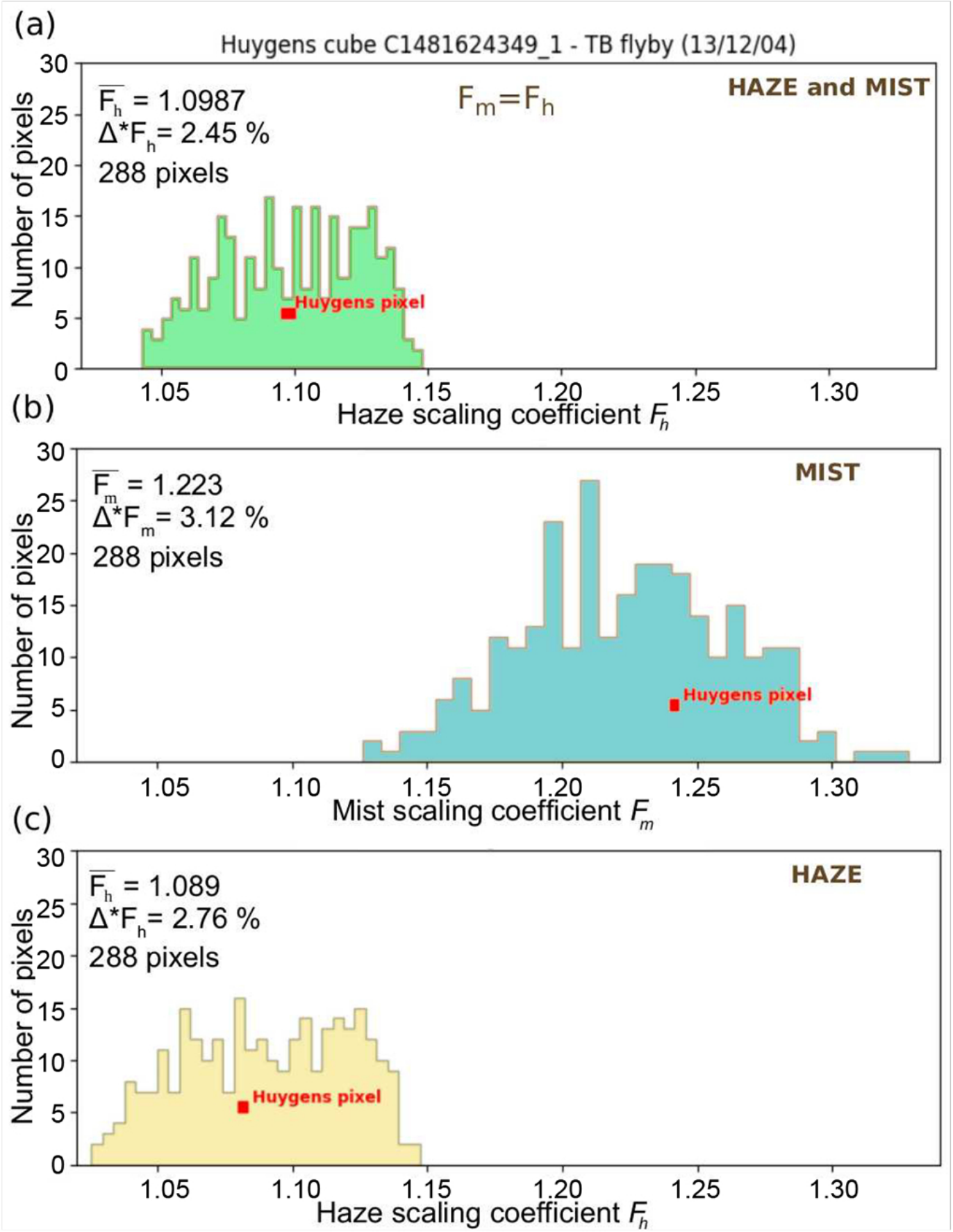
(a)
Huygens cube C1481624349_1 - TB flyby (13/12/04)
$\overline{F_h}$ = 1.0987
Δ^*F_h= 2.45 %
288 pixels
$F_m=F_h$
HAZE and MIST
Huygens pixel
Number of pixels
Haze scaling coefficient F_h
(b)
$\overline{F_m}$ = 1.223
Δ^*F_m= 3.12 %
288 pixels
MIST
Huygens pixel
Number of pixels
Mist scaling coefficient F_m
(c)
$\overline{F_h}$ = 1.089
Δ^*F_h= 2.76 %
288 pixels
HAZE
Huygens pixel
Number of pixels
Haze scaling coefficient F_h

Figure 9

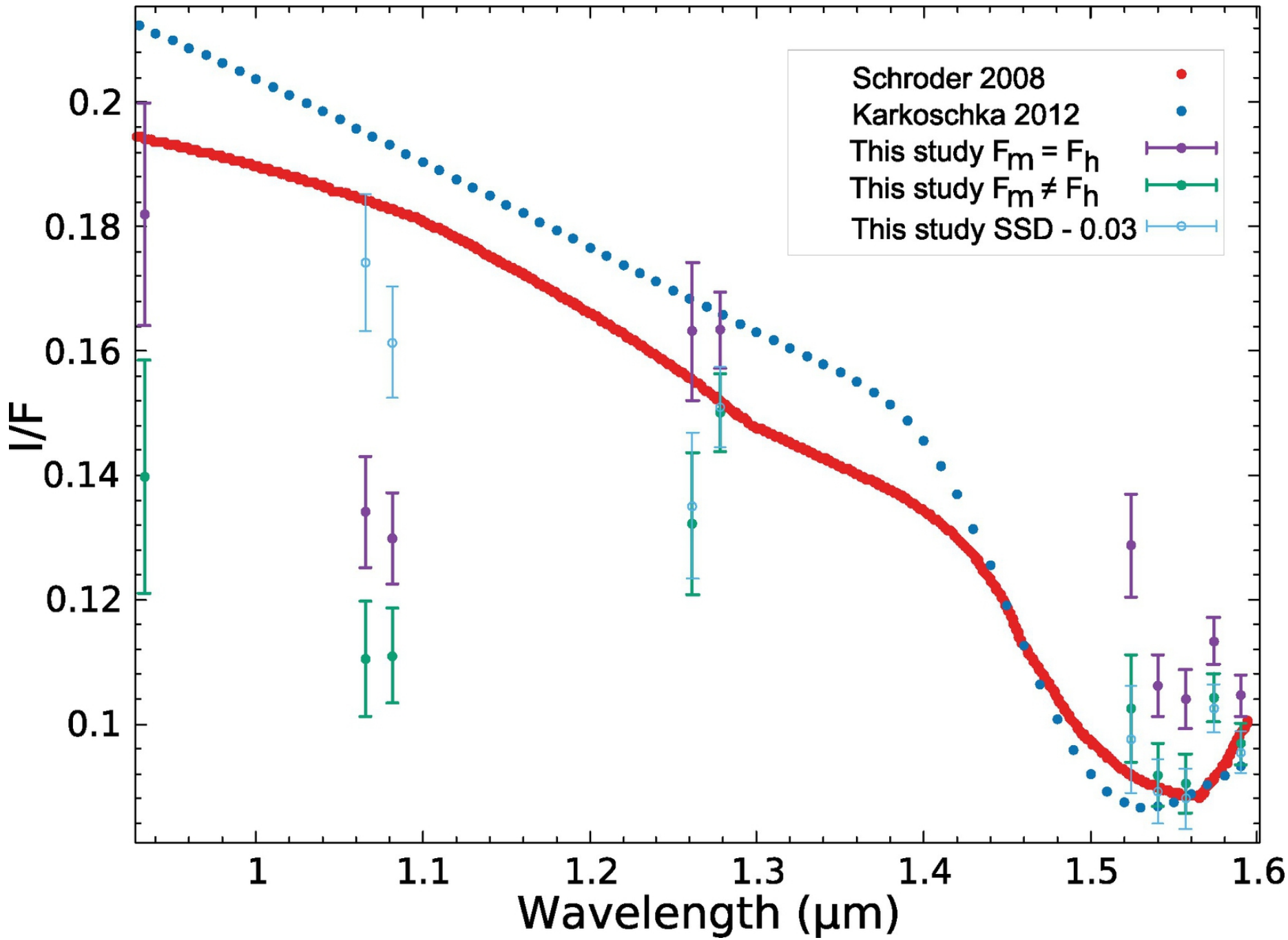
Schroder 2008
Karkoschka 2012
This study $F_m = F_h$
This study $F_m \neq F_h$
This study SSD - 0.03
I/F
0.2
0.18
0.16
0.14
0.12
0.1
1
1.1
1.2
1.3
1.4
1.5
1.6
Wavelength (μm)

Figure 10

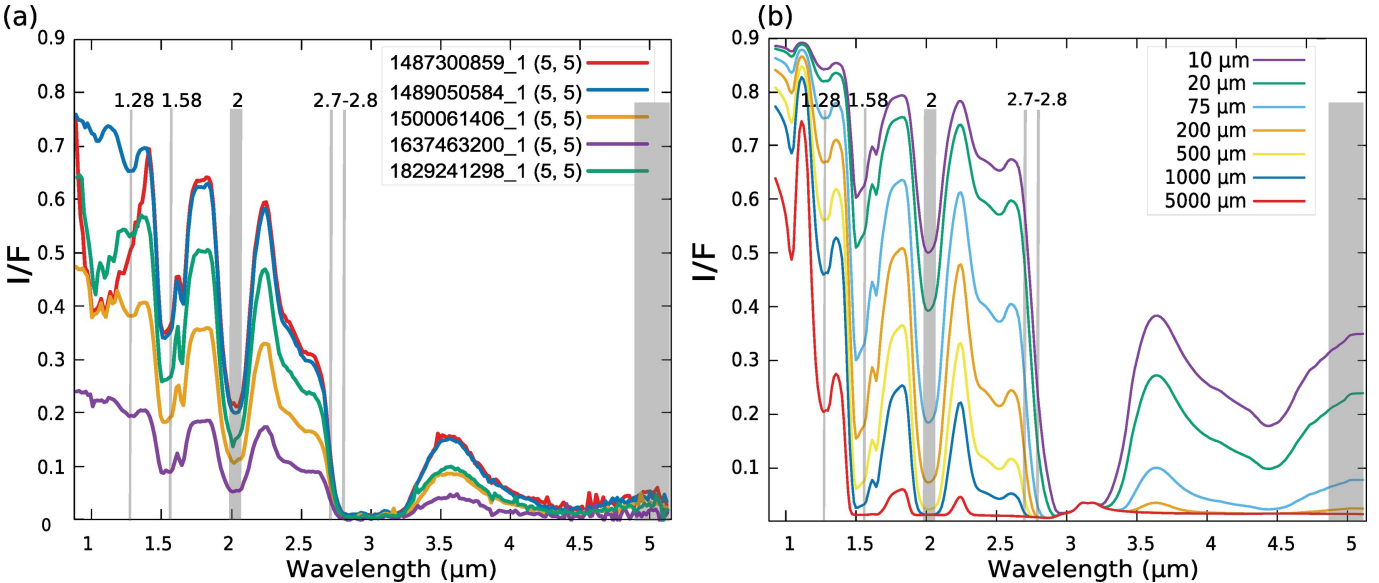
(a)
1.28
1.58
2
2.7-2.8
1487300859_1 (5, 5)
1489050584_1 (5, 5)
1500061406_1 (5, 5)
1637463200_1 (5, 5)
1829241298_1 (5, 5)
I/F
Wavelength (µm)
(b)
10 µm
20 µm
75 µm
200 µm
500 µm
1000 µm
5000 µm

Figure 11

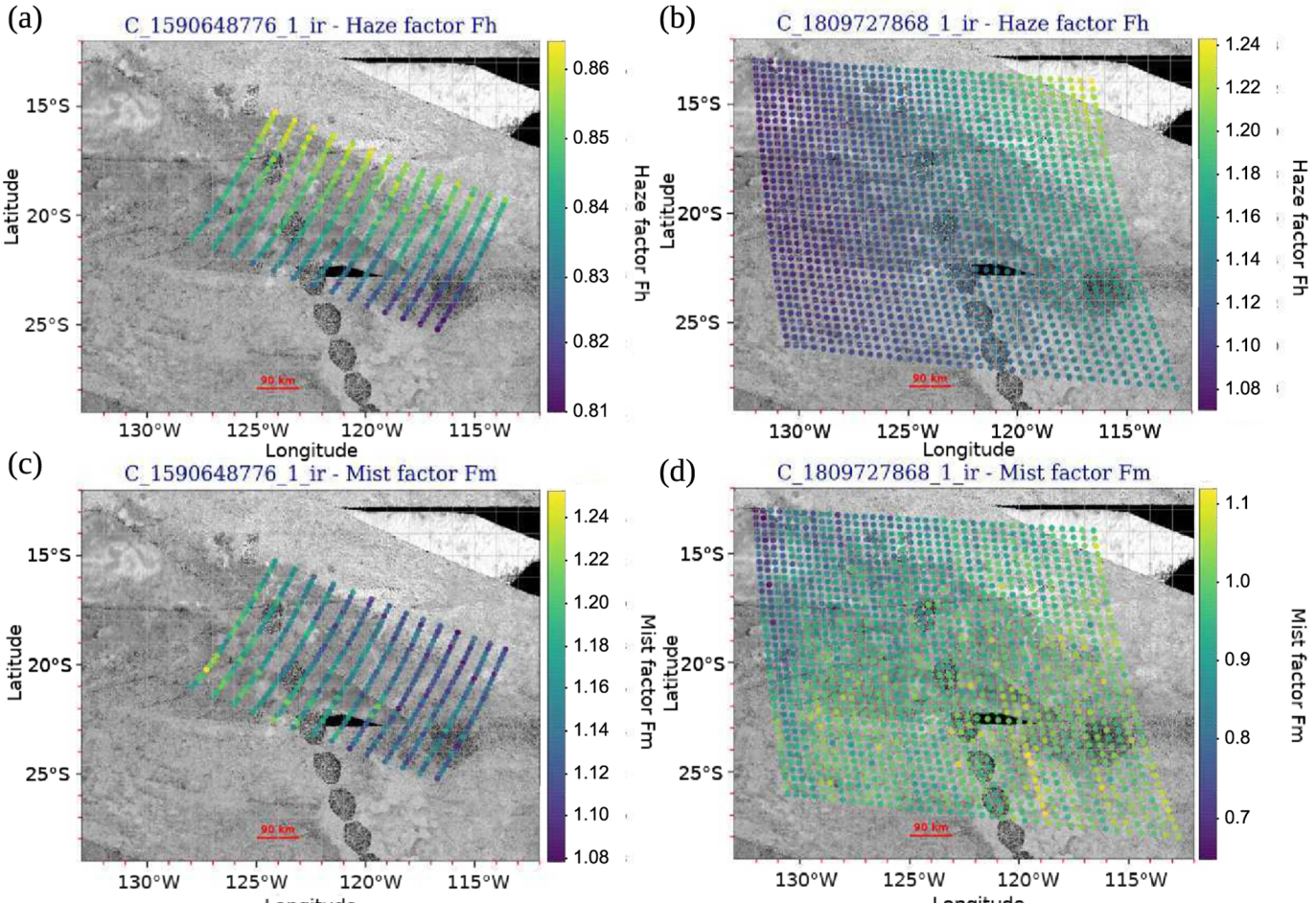
(a)
C_1590648776_1_ir - Haze factor Fh
Latitude
15°S
20°S
25°S
130°W
125°W
120°W
115°W
Longitude
90 km
0.86
0.85
0.84
0.83
0.82
0.81
Haze factor Fh
(b)
C_1809727868_1_ir - Haze factor Fh
1.24
1.22
1.20
1.18
1.16
1.14
1.12
1.10
1.08
Haze factor Fh
(c)
C_1590648776_1_ir - Mist factor Fm
1.24
1.22
1.20
1.18
1.16
1.14
1.12
1.10
1.08
Mist factor Fm
(d)
C_1809727868_1_ir - Mist factor Fm
1.1
1.0
0.9
0.8
0.7
Mist factor Fm

Figure 12

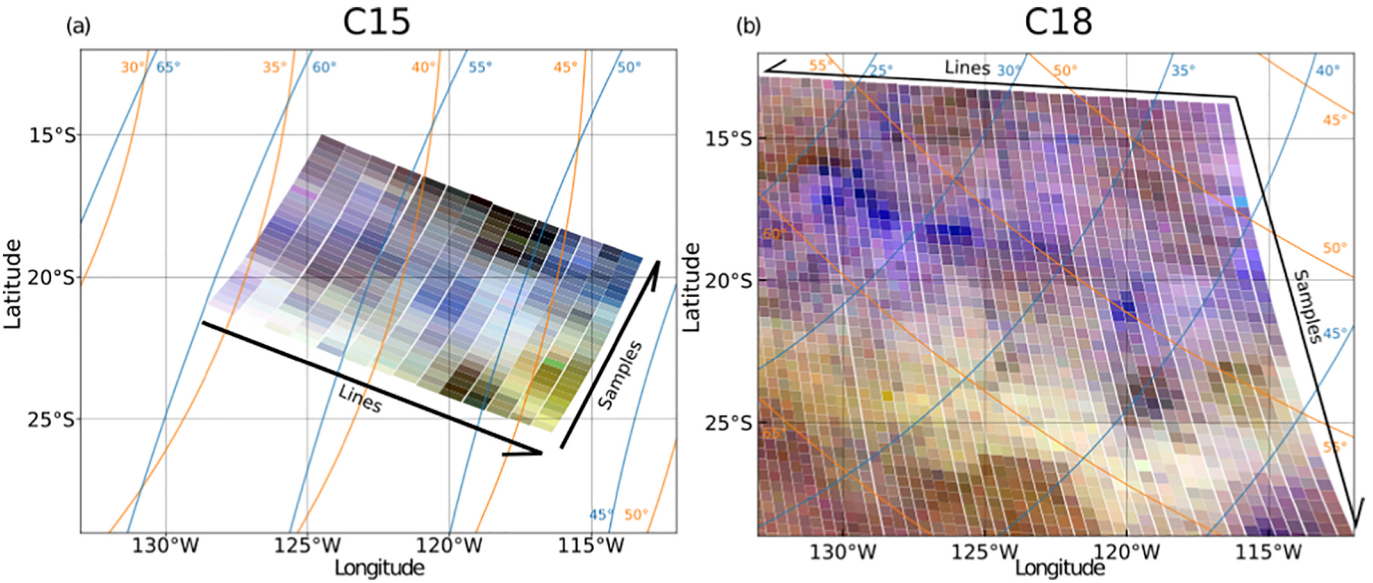
(a)
C15
30°
65°
35°
60°
40°
55°
45°
50°
15°S
20°S
25°S
Latitude
Lines
Samples
45°
50°
130°W
125°W
120°W
115°W
Longitude
(b)
C18
55°
25°
Lines
30°
50°
35°
40°
45°
15°S
20°S
25°S
Latitude
60°
50°
Samples
45°
65°
55°
130°W
125°W
120°W
115°W
Longitude

Figure 13

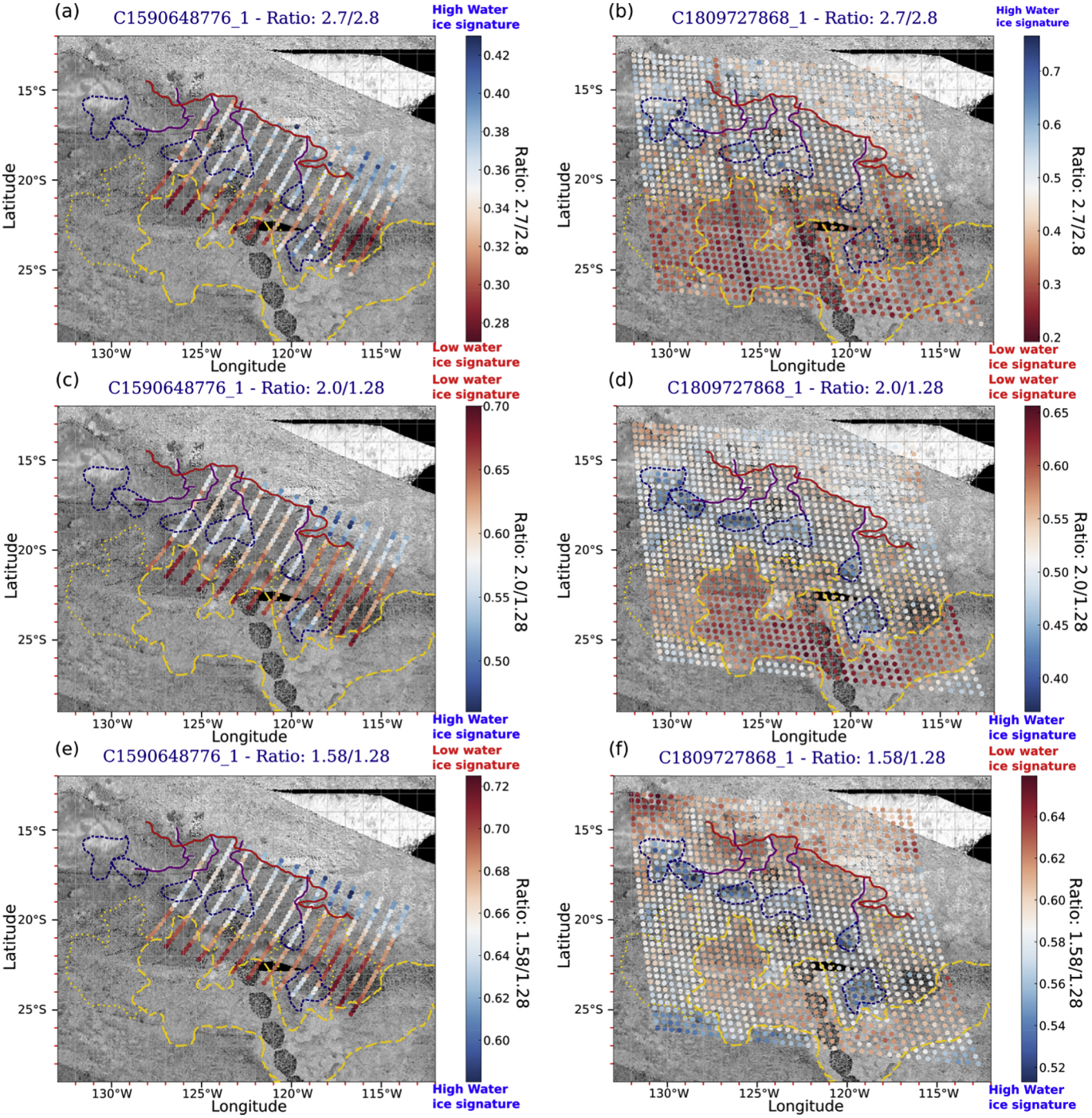
(a)
C1590648776_1 - Ratio: 2.7/2.8
High Water ice signature
Low water ice signature
Ratio: 2.7/2.8
(b)
C1809727868_1 - Ratio: 2.7/2.8
High Water ice signature
Low water ice signature
Ratio: 2.7/2.8
(c)
C1590648776_1 - Ratio: 2.0/1.28
Low water ice signature
High Water ice signature
Ratio: 2.0/1.28
(d)
C1809727868_1 - Ratio: 2.0/1.28
Low water ice signature
High Water ice signature
Ratio: 2.0/1.28
(e)
C1590648776_1 - Ratio: 1.58/1.28
Low water ice signature
High Water ice signature
Ratio: 1.58/1.28
(f)
C1809727868_1 - Ratio: 1.58/1.28
Low water ice signature
High Water ice signature
Ratio: 1.58/1.28
Latitude
Longitude
15°S
20°S
25°S
130°W
125°W
120°W
115°W

Figure 14

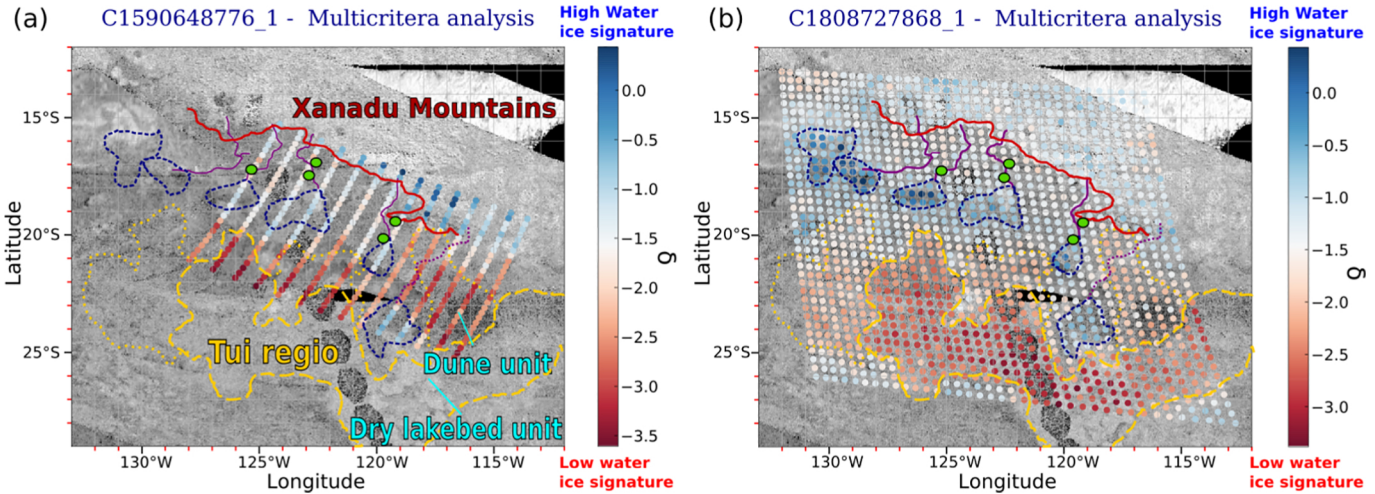
(a)
C1590648776_1 - Multicritera analysis
High Water ice signature
Low water ice signature
Xanadu Mountains
Tui regio
Dune unit
Dry lakebed unit
15°S
20°S
25°S
Latitude
130°W
125°W
120°W
115°W
Longitude
0.0
−0.5
−1.0
−1.5
−2.0
−2.5
−3.0
−3.5
δ
(b)
C1808727868_1 - Multicritera analysis
High Water ice signature
Low water ice signature
15°S
20°S
25°S
Latitude
130°W
125°W
120°W
115°W
Longitude
0.0
−0.5
−1.0
−1.5
−2.0
−2.5
−3.0
δ

Figure 15

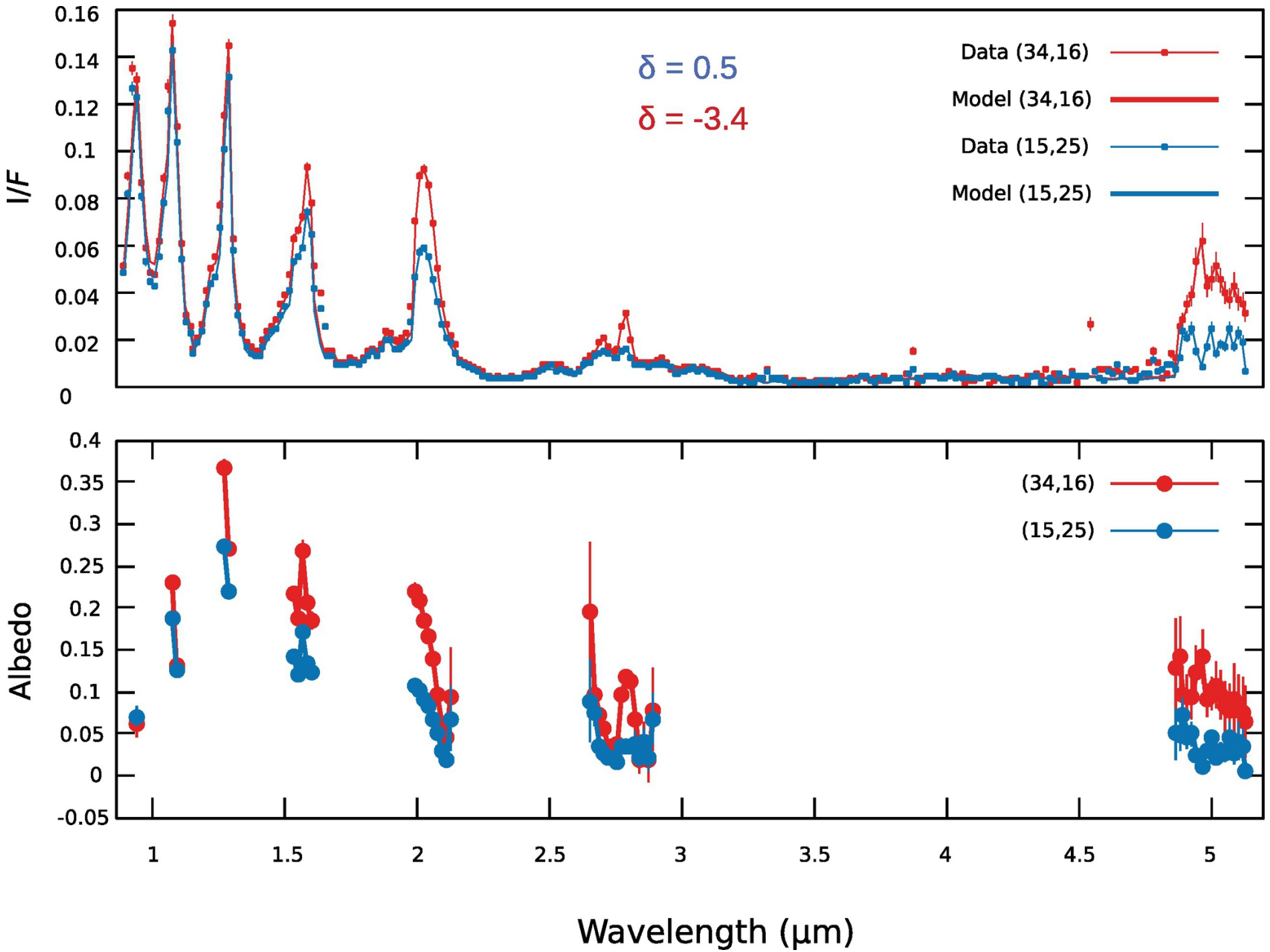
δ = 0.5
δ = -3.4
Data (34,16)
Model (34,16)
Data (15,25)
Model (15,25)
I/F
0.16
0.14
0.12
0.1
0.08
0.06
0.04
0.02
0
(34,16)
(15,25)
Albedo
0.4
0.35
0.3
0.25
0.2
0.15
0.1
0.05
0
-0.05
1
1.5
2
2.5
3
3.5
4
4.5
5
Wavelength (μm)

Figure 16

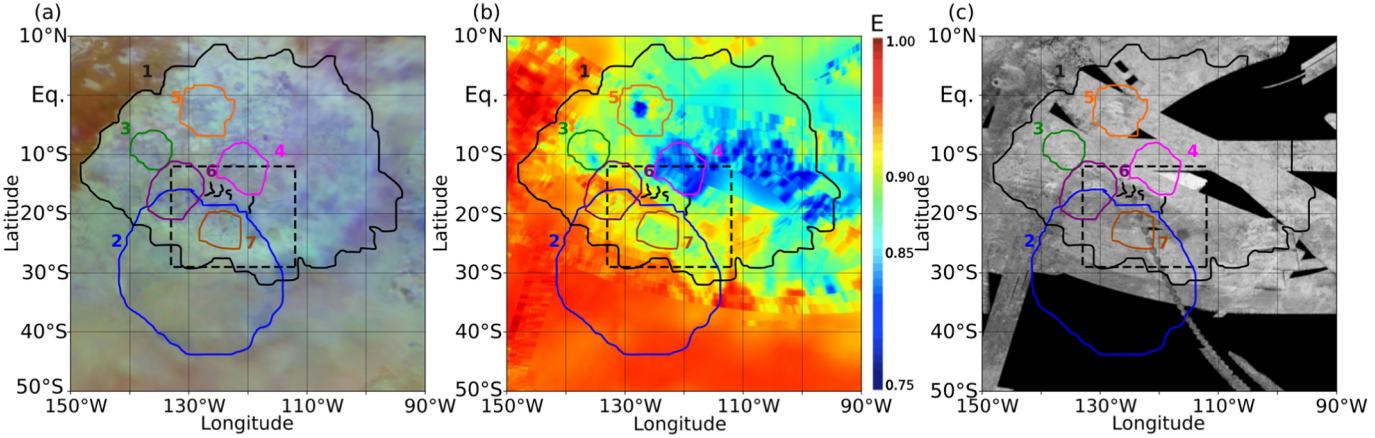
(a)
(b)
(c)
10°N
Eq.
10°S
20°S
30°S
40°S
50°S
Latitude
150°W
130°W
110°W
90°W
Longitude
1
2
3
4
5
6
7
E
1.00
0.90
0.85
0.75

Figure 17